AN ELECTRONIC BIOSENSING PLATFORM

A Ph.D. Dissertation
Presented to
The Academic Faculty

by

Ramasamy Ravindran

In Partial Fulfillment
of the Requirements for the Degree
of Doctor of Philosophy in the
School of Electrical and Computer Engineering

The Georgia Institute of Technology

August 2012

AN ELECTRONIC BIOSENSING PLATFORM

Approved by:

Dr. James D. Meindl, Advisor
School of Electrical and Computer Engineering
Georgia Institute of Technology

Dr. John F. McDonald
School of Biology
Georgia Institute of Technology

Dr. Muhannad S. Bakir
School of Electrical and Computer Engineering
Georgia Institute of Technology

Dr. Bonnie H. Ferri
School of Electrical and Computer Engineering
Georgia Institute of Technology

Dr. Gregory W. Book
Institute for Electronics and Nanotechnology
Georgia Institute of Technology

Date Approved: May 16, 2012

To my wonderful Mother and Father.

ACKNOWLEDGEMENTS

My time in graduate school has been full of people I've had great experiences with and, in countless ways, have given me great opportunities. I learned far more because of the time shared with them than I ever could have from a book, lab, or classroom.

To my Mom and Dad: *Thanks shaping me more than anyone else and for teaching me about holding true to one's principles.*

To Dr. James Meindl: *Thanks for showing me that intelligence, class, and dignity can co-exist in a life full of stories.*

To Drs. Raghu Murali, Greg Book and Muhannad Bakir: *Thanks for all great conversations about life over so many lunches and dinners.*

To GSI Mom Jennifer Root and Tina Moseley: *Thank you for conveying the spirit of the group so well.*

To Drs. John McDonald and Bonnie Ferri: *Thanks for taking the time to be a part of my committee and working with all of the graduate students in Biology and ECE.*

To Drs. Mike Hutsel and Greg Triplett: *I wouldn't be here at Tech were it not for you two. Thanks for the bike rides, the classes, and times just spent talking in Columbia and Atlanta.*

To Dr. Ron Fox: *You taught the best class I've ever had in college.*

To Dr. Ken Scarberry: *Thanks for showing me the path to logical thinking and consulting.*

To Ian Yang, Kevin Brenner, T. J. Beck, Sarah Bryan, Farhana Zaman, Jenna Fu, Gerald Lopez, and Calvin King: *It was wonderful working with you over the years and I hope to share many more memories going forward.*

To Scott Hood: *You were the perfect sounding board. I don't need to say more.*

To Jake Sadie: *You were right up there in the sounding board department.*

To Gary Spinner, Devin Brown, Joel Pikarsky, Scott Fowler, Eric Woods, Charlie Suh, John Pham, and Vinnie Nguyen: *Thanks for putting up with a guy that could occasionally be whiney but always had the best of intentions.*

To The Boston Consulting Group: *Thanks for giving me the chance to start pursuing my professional life after college.*

I'll spend the rest of my life never forgetting the people that I shared those wonderful memories with and helped me find myself as a person. It's a process that I hope never ends because there is such a magical world out there with so much to learn about. Thank you again.

TABLE OF CONTENTS

LIST OF TABLES

LIST OF FIGURES

LIST OF SYMBOLS AND ABBREVIATIONS

3DS	Three-dimensional stacking
BOE	Buffered oxide etch
BOX	Buried oxide
CMOS	Complimentary metal-oxide-semiconductor
EBL	Electron-beam lithography
ELISA	Enzyme-linked immunosorbent assay
FET	Field-effect transistor
FITC	Fluorescein isothiocyanate
FWHM	Full width at half maximum
HSQ	Hydrogen silsesquioxane
IC	Integrated circuit
ICP	Inductively coupled plasma
MEMS	Microelectromechanical systems
PBS	Phosphate buffered saline
PECVD	Plasma-enhanced chemical vapor deposition
RIE	Reactive ion etch
RTP	Rapid thermal process
SiNW	Silicon nanowire

SNP	Single nucleotide polymorphism
SOI	Silicon-on-insulator
SPION	Superparamagnetic iron oxide nanoparticles
TMAH	Tetramethylammonium hydroxide
TSV	Through-silicon via

SUMMARY

The objective of this research was to develop the initial constituents of a highly scalable and label-free electronic biosensing platform. Current immunoassays are becoming increasingly incapable of taking advantage of the latest advances in disease biomarker identification, hindering their utility in the potential early-stage diagnosis and treatment of many diseases. This is due primarily to their inability to simultaneously detect large numbers of biomarkers. The platform presented here – termed the electronic microplate – embodies a number of qualities necessary for clinical and laboratory relevance as a next-generation biosensing tool. SiNW sensors were fabricated using a purely top-down process based on those used for non-planar CMOS ICs on SOI wafers and characterized in both dry and biologically relevant ambients. Canonical pH measurements validated the sensing capabilities of the initial SiNW test devices. A low density SiNW array with fluidic wells constituting isolated sensing sites was fabricated using this process and used to differentiate between both cancerous and healthy cells and to capture superparamagnetic particles from solution. TSVs were then incorporated to create a high density sensor array, which was also characterized in both dry and PBS ambients. The result is the foundation for a platform incorporating versatile label-free detection, high sensor densities, and a separation of the sensing and electronics layers. The electronic microplate described in this work is envisioned as the heart of a next-generation biosensing platform compatible with conventional clinical and laboratory workflows and one capable of fostering the realization of personalized medicine.

1 INTRODUCTION

1.1 Pre-history of the Project

Extraordinary advances have been made over the last half-century in microelectronics and biology. Integrated circuits (ICs) have grown in complexity from tens of crudely interconnected transistors to billions of transistors capable of switching on and off in the time a photon travels a few centimeters. Meanwhile, genomics has progressed from sequencing a few thousand nucleotide bases in the simplest of viruses and microorganisms to starting to elucidate the complex interplay between the three billion base pairs in the human genome – regions of which range in purpose from being mere evolutionary remnants to the variable coding for antibodies in the adaptive immune system. Despite the tremendous progress in these two fields, there has been a negligible crossover of technology between the two until recently. As we trend towards personalized medicine, there is a tremendous opportunity for collaboration between these two historically distinct fields.

This project originated as an effort to envision a next-generation biosensing platform that takes advantage of recent developments in biology and electronics and use those developments to implement components of such a platform from both a physical entity and application point of view.

1.2 Background

Diseases perturb the normal functioning of an organism. In doing so, they trigger various measurable changes in the levels and activities of biomolecules. These changes can range from an increased production of specific antibodies in response to the common cold to a modification of the genome as a result of a retrovirus infection or cancer.

Traditionally, screening for diseases such as cancer has involved looking at one of these biomolecules or more specifically, a biomarker for a given disease. Prominent examples of biomarkers include proteins like prostate specific antigen for prostate cancer and cancer antigen 125 for ovarian cancer. Unfortunately, these and other biomarkers are nowhere near perfect indicators. Accuracy is often around 80 percent or less with a significant number of false positive and false negative results. [1-4] This can result in expensive and unnecessary further tests and treatment programs in the case of false positives or, more detrimentally, a failure to identify a disease in the case of false negatives. Both of these situations increase costs, lessen the chances for a positive prognosis, and place an undue burden on both the patient and the healthcare system. Other aggressive carcinomas like pancreatic cancer are even more challenging to detect early. At-risk patients must be regularly followed or screened for indirect markers with efficacy in both situations even poorer than with single marker screening. [5, 6]

The critical flaw in using single traditional biomarkers for each disease is that they often cannot adequately capture the incredibly large number of ways in which various diseases affect different individuals. Further, traditional biomarkers are generally not conducive to early stage detection – a time when the prognosis is usually dramatically

better. [7, 8] The resolution for this, and one that has received a tremendous amount of attention since the sequencing of the human genome, is to identify tens or hundreds of biomarkers for each disease. [9-11] By screening for an entire palette of biomarkers, a much more certain diagnosis can be made. For example, if ten biomarkers exist for a disease, a clinician could diagnose with high certainty that a patient has that disease if they exhibit seven of those biomarkers. This approach much better accommodates how different patients may express different biomarkers for the same disease.

Recent advances in genomics have enabled researchers to discover new types of biomarkers. For example, cancerous cells often feature several characteristic single nucleotide polymorphism (SNP) mutations in their DNA that can be used as effective biomarkers. [11] In fact, the entire gene expression sequence including DNA, mRNA, transcription factors, the translated proteins, and a number of other associated biomolecules is rich in potential biomarkers. [12, 13] Broadly speaking, diseases produce a wide range of biomolecules that can serve as effective indicators. These span the spectrum from nucleic acids and proteins to metabolites, carbohydrates, and even individual ions. Therefore, a useful diagnostic platform should be capable of detecting a large variety of biomarkers above and beyond the proteins that have largely served as the biomarkers in current immunoassays.

The concept of personalized medicine is idealistic, but nonetheless, is something that has marched closer and closer to realization over the last decade and will continue to do so in the decades going forward. In a world of perfect diagnoses, diseases would either manifest themselves in the same manner in all individuals or we would have the

capability to identify all possible variations of any given disease across a population. With the former clearly not being the case, researchers have turned to the later. [14]

There is a tremendous need for a next-generation biosensing platform that is capable of effectively screening for large sets of disease biomarkers – thousands or more – that more comprehensively describe numerous diseases across numerous individuals. Existing general purpose immunoassays used to detect biomarkers such as enzyme-linked immunosorbent assays (ELISAs) are typically several decades old and do not lend themselves to readily scaling to the levels needed to screen for thousands or millions of biomarkers – as would be necessary to concurrently screen for multiple cancers and other diseases. [15] Some newer technologies are scalable, but are limited in the types of biomarkers they can identify. For example, DNA microarrays can screen for thousands of SNPs, but are limited to the detection of nucleic acids. [16] Compounding this situation, nearly every clinical biosensing technology currently in use employs the use of labels such as fluorophores, radioisotopes, or enzymes which are indirect indicators of a sensing event. This adds complexity in conducting the assay and limitations in the capabilities of that assay. [17]

There is simply no highly scalable, general purpose biosensing platform currently in widespread use. A next-generation biosensing platform needs to be a substantial step forward from decades old existing technologies, take advantage of the latest developments in biology and medicine, and have broad applications. It is the objective of this research to outline such a biosensing platform and implement and demonstrate important aspects of that platform.

1.3 Sensing Methodologies

Biosensing as applied to assays generally falls into two broad categories – labeled and label-free sensing. Methodologies that are complex and reserved for low-throughput applications such as mass spectroscopy are not included in this discussion. A fundamental drawback of all labeled sensing methodologies is the finite number of different biomarkers for which they can simultaneously screen. This limitation manifests itself in a number of ways, but looking at optical labels – the most common class of labels – effectively illustrates this. All fluorophores, including commonly used ones such as cyanine and FITC, are excited around a certain wavelength and emit around a different, longer and lower energy, wavelength. The emission wavelength of all fluorophores is not a discrete peak, but rather a spectrum with a peak at a given wavelength and a FWHM spanning tens of nanometers to either side. This has not been a limitation in classical immunoassays that screen for less than a handful of biomarkers as there can be sufficient separation of the emission spectra of different fluorophores to uniquely identify them. However, at some point, and generally at fewer than ten different fluorophores in the visible wavelength region, the emission spectra of a given fluorophore begins to overlap with that of its neighbors sufficiently enough that they become increasingly difficult to distinguish. [18]

One solution would be to use a combination of fluorophores or multiplexing to form more unique fingerprints. Protein microarrays often employ this, but even then they are only able to push this limit out to a few hundred different biomarkers while incurring penalties in the time and cost brought on by the procedures used to combine multiple optical labels prior to the assay and then detect them afterwards. [19, 20]

Another logical solution would be a label that has a near-discrete emission spectrum. Quantum dots offer this capability in principal, but in practice, variance in composition and size effectively limit quantum dots, even those that have multiplexed signatures, to a few thousand discernible labels. [21, 22] Other labeled approaches ranging from those using radioisotopes to surface enhanced Raman spectroscopy suffer from similar limitations. [23] Additionally, all labeled sensing methodologies require additional processing steps beyond the initial biomarker capture event and these steps only become increasingly involved and costly as multiplexing measures are introduced to better distinguish between an increased number of biomarkers.

Looking at one of the most commonly used conventional labeled methods, ELISA, highlights these drawbacks. The process is depicted in Figure 1.1.

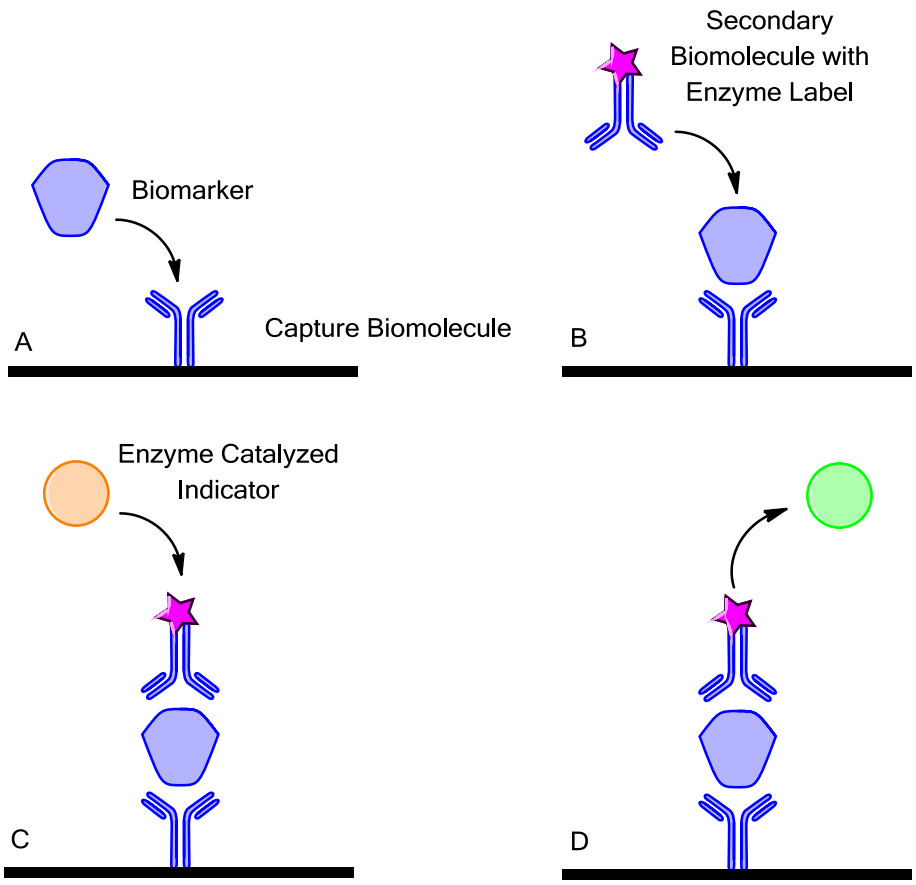

Figure 1.1: A schematic depiction of ELISA

ELISA starts off by binding a capture biomolecule, generally a primary antibody, to a substrate, usually a microplate. The microplate is then washed to remove any unbound primary antibody and blocked with a blocking agent to prevent non-specific binding of subsequent biomolecules. The sample, which may or may not contain the biomarker or antigen, is then introduced (A). If the antigen is present, the primary antibody captures it by one particular epitope or location on the antigen (B). The microplate is again washed and a secondary antibody is introduced. If the antigen is present, it binds to a different epitope on the antigen. The distinction between the primary and secondary antibodies is that the secondary antibody has attached to it an

enzyme label. After once more washing the microplate, an indicator chemical is introduced that undergoes a catalytic color change in the presence of the enzyme on the secondary antibody (C and D), thereby indicating the presence or absence of a biomarker antigen.

ELISA is a robust, ubiquitous, and low-cost assay, but in its most common form, it can only be used to screen for one or a few proteins at a time. Even newer implementations of ELISA using multiplexed fluorophore labels are bound by the limitations common to all labeled sensing methods and come at the cost of increasing the processing steps involved. [24] Unfortunately, from Raman to fluorophores, the greater number of distinct biomarkers a particular labeled scheme is able to identify, the more disproportionally complex it becomes. [18]

A next-generation biosensing platform should be unencumbered by any such limitations. It should have no fundamental upper limit to the number of distinct biomarkers that can be simultaneously screened and should also ideally require fewer processing steps than current methodologies. There has been substantial progress over the last decade to that end with the result being the development of numerous label-free methodologies. [25-29] A label-free sensor detects a property inherent to the captured biomarker, effectively detecting the primary biomarker binding event itself and not a secondary binding event as is the case with label based sensors. Because of this underlying characteristic, label-free sensors can detect an unlimited number of distinct biomarkers in a single assay given their complementary capture biomolecules. The following figure depicts the point at which a biomarker capture event can be detected in labeled and label-free sensing. In this case, the capture and secondary biomolecules are

depicted as antibodies and the biomarker as an antigen protein but this principle extends to schemes involving other biomolecules such as nucleic acids. In the case of the labeled method, this is a best case scenario – often subsequent steps are needed as is the case for methods like ELISA.

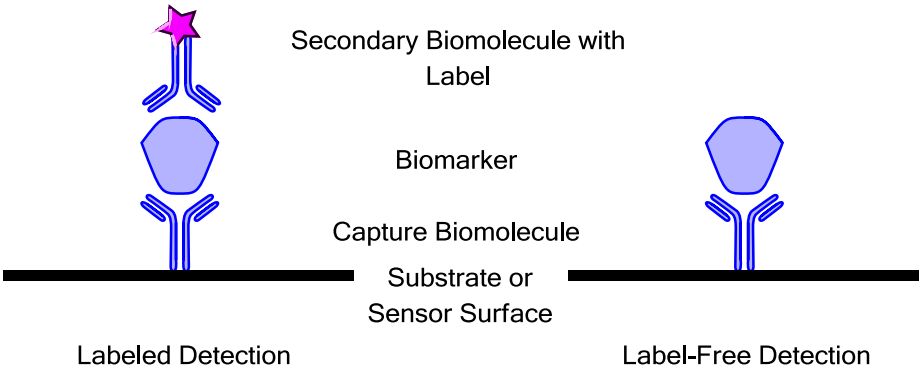

Figure 1.2: Simplified depiction of labeled detection and label-free detection

Biomarkers generally have one or both of two properties – charge and mass. For example, nucleic acids have a negative charge due to the phosphate groups on the ribose backbone. Other macromolecules such as proteins carry a charge based on where their isoelectric point, pI, is relative to the pH of the solution they are in. Similarly, a host of other disease biomarkers of interest such as ions and metabolites also carry an electric charge. The complex nature of many biomolecules also confers on them a substantial mass. Proteins and nucleic acid sequences of note as biomarkers are often tens or hundreds of thousands of daltons.

To better understand the origin of this charge and mass, let us look at an arbitrary amino acid sequence and one of the mRNA sequences that codes for one of

those amino acids. First is a sequence of arginine and glutamic acid representative of a portion of a protein. At a biological pH of 7.4, such as that of phosphate buffered saline (PBS), the arginine NH group highlighted in red is protonated to NH_2^+, lending arginine an overall positive charge. Similarly, the glutamic acid OH group highlighted in blue is deprotonated to O^-, lending glutamic acid an overall negative charge. Since proteins such as antibodies are long sequences of amino acids, these charges are summed and become a detectable characteristic of the protein sequence, provided the protein is in a solution with a pH not equal to its pI, at which point the overall protonation and deprotonation of all the amino acids lends the protein a net neutral electric charge.

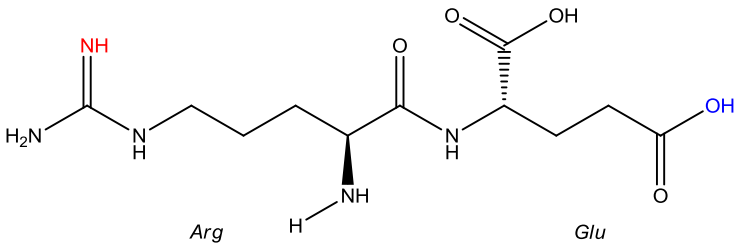

Figure 1.3: Two amino acids (arginine and glutamic acid)

DNA and mRNA also carry a net charge, but for both, this charge is negative. To see this, we can look at a short sequence of mRNA (CGU) which codes for arginine in Figure 1.4. The backbones of DNA and mRNA are comprised of ribose sugars linked by phosphate groups. These groups, highlighted in blue, carry a negative charge because of the single bonded O. This charge is similarly summed over the length of the sequence and is a detectable characteristic of the amino acid.

It should also be evident from these two examples that biomolecules also have a significant mass. For example, the amino acids in Figure 1.3 have masses of ≈174 and ≈147 Da, respectively while the bases in Figure 1.4 have masses of ≈111, ≈151, and ≈112 Da.

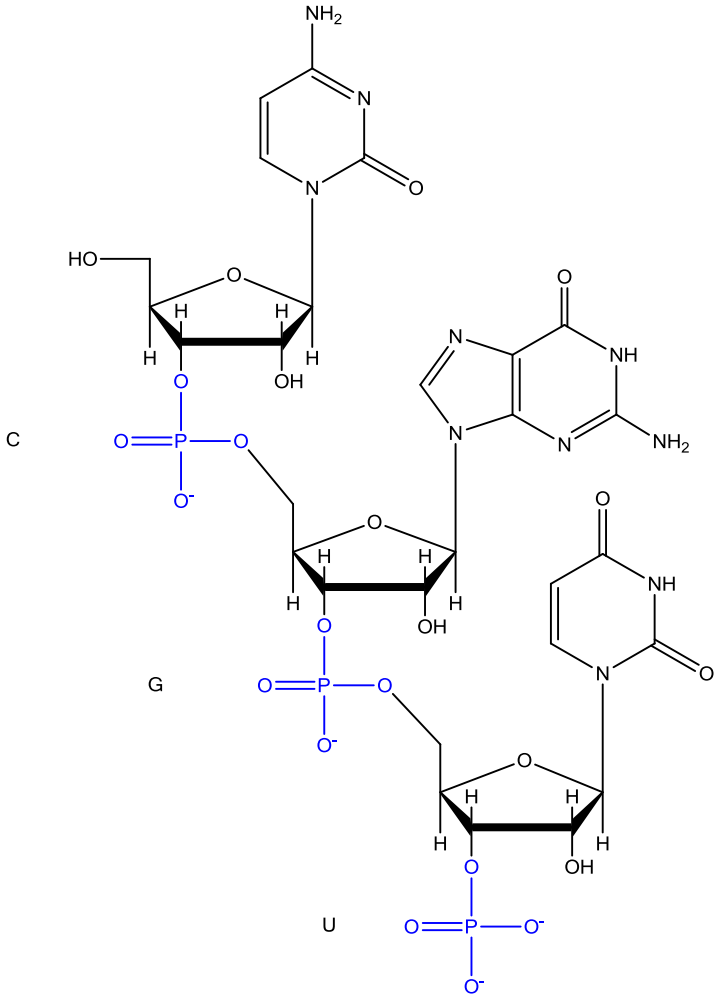

Figure 1.4: A sequence of mRNA (3'-5' CGU)

Since label-free sensing is centered on directly detecting a captured biomarker without an intermediary label, mass and charge, both being in notable abundance in

macromolecules comprised of tens to thousands of amino acids and bases or other constituents, are the most common candidate properties. Both of these approaches minimize processing steps and avoid any limitation in the number of different biomarkers that can be simultaneously detected.

Mass based sensing is outside the scope of this research, but a cursory discussion is useful. There are several variations of mass-based sensors, but typically the mass of the captured target biomolecule results in the deflection of a cantilever, the alteration of a propagating acoustic wave, or a change in oscillator resonance properties, be they mechanical or optical. [28, 30-33]

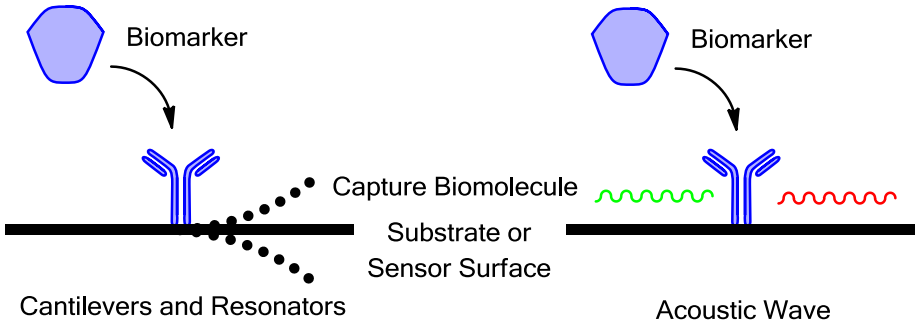

Figure 1.5: Depiction of mass based sensors

On the left, a captured biomarker results in either a deflection of a cantilever or a change in the resonance of a resonator. On the right, a captured biomarker alters an acoustic wave traveling from left (green) to right (red).

While their operating principles are sound, mass based sensors do have some drawbacks. They are fabricated using MEMS processes, are fabricated on piezoelectric substrates, or are fabricated using even more exotic methods in the case of optical

resonators. [28, 30, 32, 33] This adds a level of complexity and cost to their fabrication since they cannot be made using traditional cost-effective complimentary metal-oxide-semiconductor (CMOS) workflows. In many cases, various performance metrics of mass based sensors such as the quality factor of resonators degrades in biologically relevant environments such as aqueous solutions either by dampening or absorption. [28, 33] The actual sensing process is also quite complex and involved, requiring a combination of oscillators, transducers, filters, lasers, and high frequency electronics. [28, 30-33] While mass based sensing does have potential applications, because of the focus on CMOS workflow compatibility and scalability, this research uses charge based sensing.

Charge based sensors are generally constructed from semiconductors and are operated like conventional transistors. [26, 27, 29, 34] The charge that a captured biomarker imparts on the surface of a semiconductor modulates the current flowing from source to drain through either an inversion or accumulation channel, much as the bias on a gate does in a field-effect transistor (FET). A substantial advantage of a properly implemented charge based sensor is its compatibility with top-down CMOS fabrication workflows because of this similarity with FETs.

In this work, a silicon nanowire (SiNW) is used as the specific implementation of charge based sensing. A SiNW based sensor is of particular interest because biomolecules can be bound not just to one face of the channel as in planar devices, but to the sides as well. [26] This allows for superior modulation of I_D. Further, commercially fabricated IC FETs are trending away from planar devices and towards non-planar multigate or gate-all-around designs that closely resemble SiNWs. [35, 36]

This CMOS industry movement means that a SiNW label-free biosensor can be readily fabricated using emerging CMOS fabrication workflows.

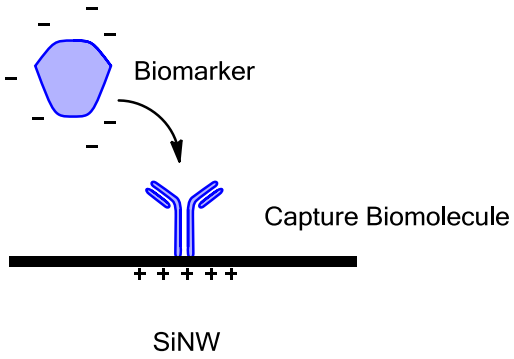

Figure 1.6: Depiction of a SiNW sensor

A negatively charged biomarker that is captured on the surface of the sensor induces a positive charge within the SiNW.

1.4 Principles of Operation for a SiNW Sensor

To better understand the principle of operation of a charge based SiNW biosensor, consider a uniformly doped SiNW operated as a majority carrier accumulation mode device in the linear region. [37, 38] The total current density reduces to the majority carrier drift current density and is given as:

$$J_{drift} = q \cdot \mu \cdot n_o \cdot E \tag{1.1}$$

where q is the elementary charge, μ is the majority carrier mobility, n_o is the majority carrier concentration, and E is the electric field. The total current for a SiNW with a rectangular cross-section is:

$$I_{drift} = J_{drift} \cdot (h \cdot w) = q \cdot \mu \cdot n_o \cdot E \cdot (h \cdot w) \tag{1.2}$$

Where h is the height of the SiNW and w is the width of the SiNW.

If we assume q, μ, and E to be fixed, then any change in current in the linear region must be the result of a change in the carrier concentration, Δn:

$$\Delta I_{drift} = q \cdot \mu \cdot \Delta n \cdot E \cdot (h \cdot w) \tag{1.3}$$

If we assume that any change in n is the result of surface charges, then Δn is equal to:

$$\Delta n = \sigma \cdot \frac{2 \cdot (h + w)}{q \cdot h \cdot w} \tag{1.4}$$

where σ (q/cm^2) is the surface charge density. When a SiNW is used as a biosensor, σ is the surface charge density that bound biomolecules impart on the SiNW. Thus, the change in current through a SiNW is:

$$\Delta I_{drift} = q \cdot \mu \cdot [\sigma \cdot \frac{2 \cdot (h + w)}{q \cdot h \cdot w}] \cdot E \cdot (h \cdot w) \tag{1.5}$$

The net current through a SiNW can be described by the following equation: [37]

$$I_{drift,net} = I_{drift} + \Delta I_{drift} = q \cdot \mu \cdot [n_o + \sigma \cdot \frac{2 \cdot (h + w)}{q \cdot h \cdot w}] \cdot E \cdot (h \cdot w) \tag{1.6}$$

where n_o ($electrons/cm^3$) (is the doping density of the SiNW. Naturally, the capture biomolecule itself will have some charge. For the purposes of simplicity, it is assumed that all effects of the capture biomolecule's charge are incorporated into n_o and that σ is only the change in effective surface charge as a result of the captured biomarker. This treatment only holds true in the linear region of operation and not in sub-threshold or saturation. A treatment of the exponential response in the sub-threshold region and the challenges associated with operation of a SiNW sensor in this region and real-world considerations associated with operation in the saturation region are given in Chapter 2.

In this first principles calculation, the change in the current flowing through the channel in a SiNW biosensor is purely the result of the change in surface charge density

or, more specifically, the change in the effective surface charge imparted by captured or proximal biomarkers. In discussions in subsequent chapters, $I_{drift,net}$ will simply be referred to as I_D – the measured drain current.

1.5 High-Level Design Considerations

In designing and using a charge based sensor, we have some fundamental considerations and some practical considerations. Let us look at considerations regarding the SiNW itself. In designing the SiNW, sensitivity should be maximized. Sensitivity, S, is simply the change in current for a given σ:

$$S = \frac{\Delta I_{drift}}{I_{drift}} = \frac{\sigma \cdot 2 \cdot (h + w)}{n_o \cdot q \cdot h \cdot w} \tag{1.7}$$

Clearly either the denominator must be minimized or the numerator maximized to maximize sensitivity. σ is determined by the biomarker and cannot be changed. q is a fundamental constant and also cannot be changed. n_o can be lowered by using a lower doping density. Limits on the minimum measurable I_D at a given V_{DS} impose some lower doping threshold, but in general, lower doping densities are preferred. Also, we notice that decreasing h and w, that is making the SiNW cross-section smaller, also improves sensitivity. Process limitations might introduce undesired effects such as surface roughness that begin to degrade performance, but again, in general, smaller cross-section SiNWs are preferred. Initial experiments in scaling placed a lower limit on SiNW width – again something discussed in Chapter 2.

These points combined do touch upon a key practical difference between top-down and bottom-up fabrication of SiNWs. Controlling process parameters such as SiNW doping concentration and dimensions are critical for consistent sensitivity.

Bottom-up grown SiNW biosensors have substantial variances in device-to-device performance because of their inherent lack of control in processing. [26] Top-down SiNW biosensors have fared substantially better because of their basis on tried and true CMOS compatible materials and workflows. [29] It is for this reason that this work centers on a CMOS compatible top-down fabrication process.

The primary reason for making a distinction between the charge of a biomolecule and the effective surface charge in earlier discussions is because of Debye screening. In any ionic solution, ions in the solution will screen all the charge of a biomolecule given a sufficient distance. This distance is known as the Debye length, λ_D, and is described by the following formula: [39]

$$\lambda_D = \frac{1}{\sqrt{4 \cdot \pi \cdot l_B \cdot \sum_i \cdot \rho_i \cdot z_i^2}} \tag{1.8}$$

Where l_B is the Bjerrum length (nm), ϱ_i is the density of each type of constituent ion (q/nm^3), and z_i is the valency of each constituent ion (dimensionless). l_B accounts for the permittivity and temperature of the solution as well as the Boltzmann constant and elementary charge. For water based solutions at 300 K, l_B is ≈0.7 nm. [39]

The Debye length is of importance because in a sufficiently strong ionic solution, much of the charge of a captured biomarker will be screened before it can have any effect on σ and therefore, I_D, Conversely, in a sufficiently weak ionic solution, spurious charges from biomarkers in solution that are not actually bound to the capture biomolecule will result in erroneous changes in I_D. [38, 39] Selection of a specific ionic strength for the buffer solution, which in turn determines a specific λ_D, is dependent on a number of factors including the charge and size of the biomarker. As such, specific

discussions of ideal PBS concentrations will be made in Chapters 3 and 4, which deal specifically with biosensing.

The surface potential effected by a charge for a given bulk and surface proton concentration is given by the Nernst equation: [40]

$$\phi = \frac{k_B \cdot T}{q} \cdot \ln\left(\frac{H^+_{bulk}}{H^+_{surface}}\right) \tag{1.9}$$

Where k_B is the Boltzmann constant (eV/K), T is the temperature (K) and the H^+s are the bulk and surface proton concentrations (q/cm^3). It follows from this that the maximum change in surface charge for a given change in pH (or put another way, a logarithmic or ten-fold change in proton concentration) is: [40]

$$\Delta V/\Delta pH = \frac{k_B \cdot T}{q} \cdot \ln(10) \tag{1.10}$$

Which at 300 K equates to 59 mV/pH; this being the classically fundamental limit on the sensitivity of an ion-gated FET. The discussion of the Nernst limit is purely academic for the purposes of this work because the fabricated devices are limited more by the SiNW cross-sectional area and doping concentration, which combined do not allow complete modulation of carriers through the entire SiNW. [41]

1.6 High-Level Usability Considerations

While performance is a fundamental consideration, usability is a practical one. A new platform should only require minimal changes in assay workflows for clinicians and researchers. It should also be low-cost. Conceptually, an ideal starting point is to view this new platform as a highly scaled version of the most ubiquitous of current platforms, the conventional microplate. [42]

To better understand the rationale for using a microplate as the basis, we can look at an alternative approach for sample delivery, microfluidics; an area that has received a fair amount of attention. [43] Elaborate on-chip routing of fluids has been demonstrated. [44] On-chip micofluidics, however, come with several drawbacks. They increase the cost and complexity of the chip and also require off-chip control elements such as pumps. [44, 45] However, most important is the issue of fluid flow in increasingly narrow microfluidic channels. As flow starts to become diffusion dominated, delivering analyte to individual sensors becomes exceedingly prohibitive in terms of both time and sensitivity. [46] The flux of analyte molecules in microfluidic systems decreases dramatically compared to macro-scale alternatives and in fact places a practical lower limit around femtomolar sensitivities even for fluidic channels hundreds of microns wide. [47] For these reasons, the logical solution is to turn to spotting individual wells in a manner similar to how protein microarrays are spotted – and something that is also a scaled analog of the micropipettes used to load conventional microplates. [19] Isolated wells can also be lithographically defined and the fabrication of an electronic microplate using wells remains CMOS compatible, something that would not be the case with microfluidics. Such a solution could also potentially be used in flow-through systems if the application arises.

1.7 The Electronic Microplate

Vital to the realization of the electronic microplate is coalescence of a number of technologies. Many of these concepts have been previously demonstrated piecemeal. For example, arrayed SiNWs made with bottom-up processes have been used to detect

conventional cancer markers. [48] However, this has not been accomplished with a top-down fabrication process. CMOS compatible SiNW biosensors have been demonstrated, but not in an arrayed fashion. [29] This work aims to develop both new applications and certain enabling technologies for a platform that best leverages an electronic label-free sensor – a platform that can ultimately be scalable, versatile, and practical.

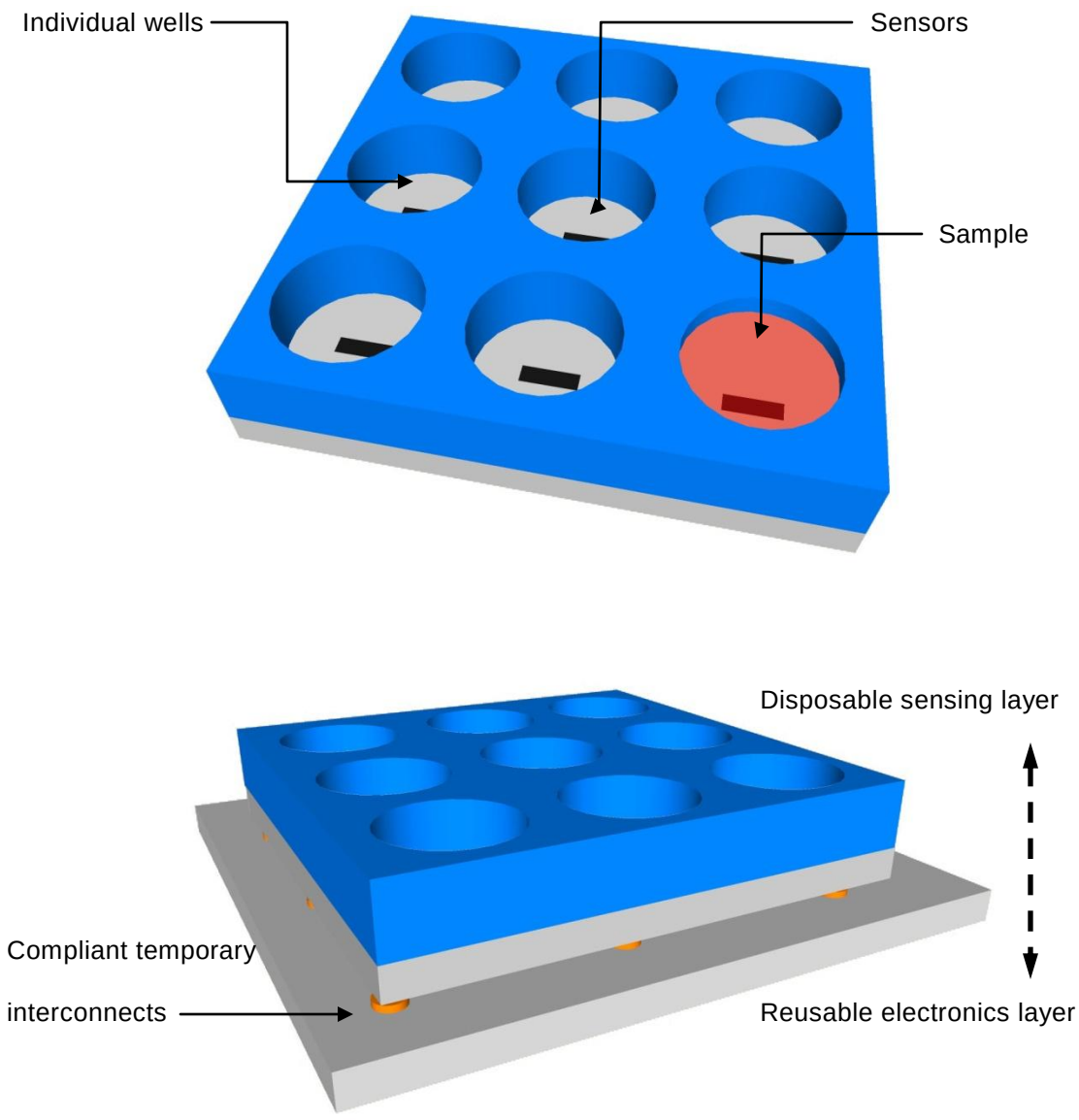

Figure 1.7: The electronic microplate in an example 3 x 3 configuration

The electronic microplate can be described as a modern, label-free, high-density, and electronic reincarnation of the ubiquitous and five decade old conventional microplate. In this sense, the electronic microplate consists of individual isolated wells, each containing a SiNW sensor. These sensors are individually addressable and therefore capable of concurrently performing multiple assays.

This approach maximizes the usability of the platform. However, there is another key piece of technology necessary to truly enable a platform with broad utility as the electronic microplate should be low-cost and disposable. This requires a separation of the electronic microplate or sensing layer from the sensing electronics or electronics layer and linking the two via temporary compliant interconnects. Three-dimensional stacking (3DS) technologies, in particular the use of through-silicon vias (TSVs), can be used to electrically connect the wet sensing side of the sensing layer to the dry interface side and compliant interconnects to mate the dry side interface side of the sensing layer with the electronics layer. [49, 50]

A number of direct and indirect advantages are the result. First, costly sensing electronics can be reused, lowering the cost of the disposable portion. Second, routing the signals directly to the backside allows for exceptionally high sensor densities. Third, the wet sensing side is delineated from the sensing electronics. Fourth, usage of the chip remains very much in line with existing clinical workflows. Fifth, chips with a broad range of capabilities including heaters for polymerase chain reactions and SiNWs for biomarker detection can potentially be interchangeable. In the spirit of systems biology, these advantages could combine to create tremendous potential for widespread applications ranging from point-of-care diagnostics to fundamental research. [51, 52]

1.8 Overview of the Presented Research

The electronic microplate is a coherent concept, but requires the combination of many technologies across many fields. While the idea is in its infancy, the purpose of this work is two-fold: demonstrate new label-free sensing methodologies that when combined with previously demonstrated methodologies can add to the modern diagnostic toolkit and demonstrate a promising scaling path forward that can ultimately enable ubiquitous screening for countless biomarkers. To that end, it focuses on the sensing layer of the platform and assays that can be performed on it.

This dissertation focuses on two main areas: new biosensing applications for SiNW sensor arrays and scaling SiNW sensor arrays. The associated work is divided into four chapters. The first of these, Chapter 2, discusses the development of a baseline workflow for the fabrication of SiNW sensors and measurement methodologies congruent with non-planar CMOS fabrication – neither of which existed prior in the facilities used for this work. The next three chapters discuss new sensing methodologies and scaling. Chapter 3 discusses using a fully top-down fabricated SiNW sensor array with integrated wells to delineate between cancerous and non-cancerous cells using their intracellular contents. [53] Chapter 4 discusses using this same array to sense the presence of superparamagnetic particles in solution. [54] Then Chapter 5 discusses the use of TSVs to dramatically increase SiNW sensor densities in a truly scalable manner. [55] A final chapter wraps up with the contributions of this work and points out the logical next steps and areas of collaboration necessary to implement the electronic microplate concept as a next-generation biosensing platform.

2 SiNW CONSIDERATIONS AND PROCESS DEVELOPMENT

2.1 Background

The initial priorities of the presented research were to establish a baseline SiNW fabrication workflow and a set of measurement parameters. Working from the ground up with both applications and scaling in mind painted a picture where fabrication and measurement considerations were the initial drivers.

This chapter discusses three topics. The first topic discusses the design and fabrication of the SiNW test devices that formed the basis for all subsequent testing in this work. The second topic summarizes the considerations that went into how the electrical measurements were performed. The third topic recounts the electrical characterization of these devices in dry and wet conditions.

2.2 Process Development

The first step in the process development was to create a highly anisotropic etch that could define the nanometer scale features required for the SiNWs. This eliminated wet etches such as those using TMAH which etch different crystal planes at greatly different rates. [56] Attention logically turned to using a dry inductively couple plasma (ICP) based process. [57] Test patterns consisting of 100 nm, 50 nm, 25 nm, and 15 nm lines were patterned with electron-beam lithography (EBL), (JEOL JBX-9300FX), using hydrogen silsequioxane (HSQ) resist (Dow Chemical) on silicon-on-insulator (SOI) wafers (SOITEC) with a 70 nm thick device layer (p-type, 1-10 Ω-cm), a 145 nm buried oxide (BOX) layer, and a 500 μm handle layer. The test pattern is shown in Figure 2.1.

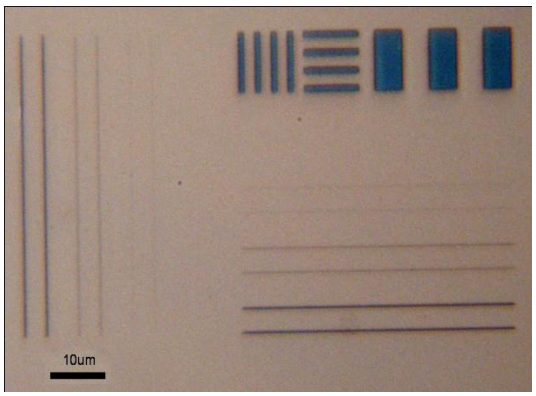

Figure 2.1: High-contrast optical image of the SiNW test pattern

The pattern is HSQ on Si. The lines are 100, 50, 25, and 15 nm in width from left to right and from bottom to top. The 15 nm lines are not visible due to the resolving limits of the microscope. The larger features at the top right were used to study EBL proximity effects. The scale bar is 10 μm.

The device layer was etched with an Ar/Cl_2 ICP (STS SOE) to the BOX, thereby forming the SiNWs. Testing indicated that the ICP process had a Si:HSQ etch selectivity of 3.69:1 nm/s (see Appendix Table 7.1). With a 70 nm device layer, the minimum HSQ thickness could only be approximately 19 nm and still suffice as an etch mask. In theory, this should have allowed for patterning 25 nm lines and perhaps even 15 nm lines without isotropy or over-etching with the thickness dependent resolution of HSQ. [58] However, real-world conditions were not quite so accommodating and 50 nm became the ideal reliably definable SiNW width. The three narrowest widths fabricated are shown in Figure 2.2.

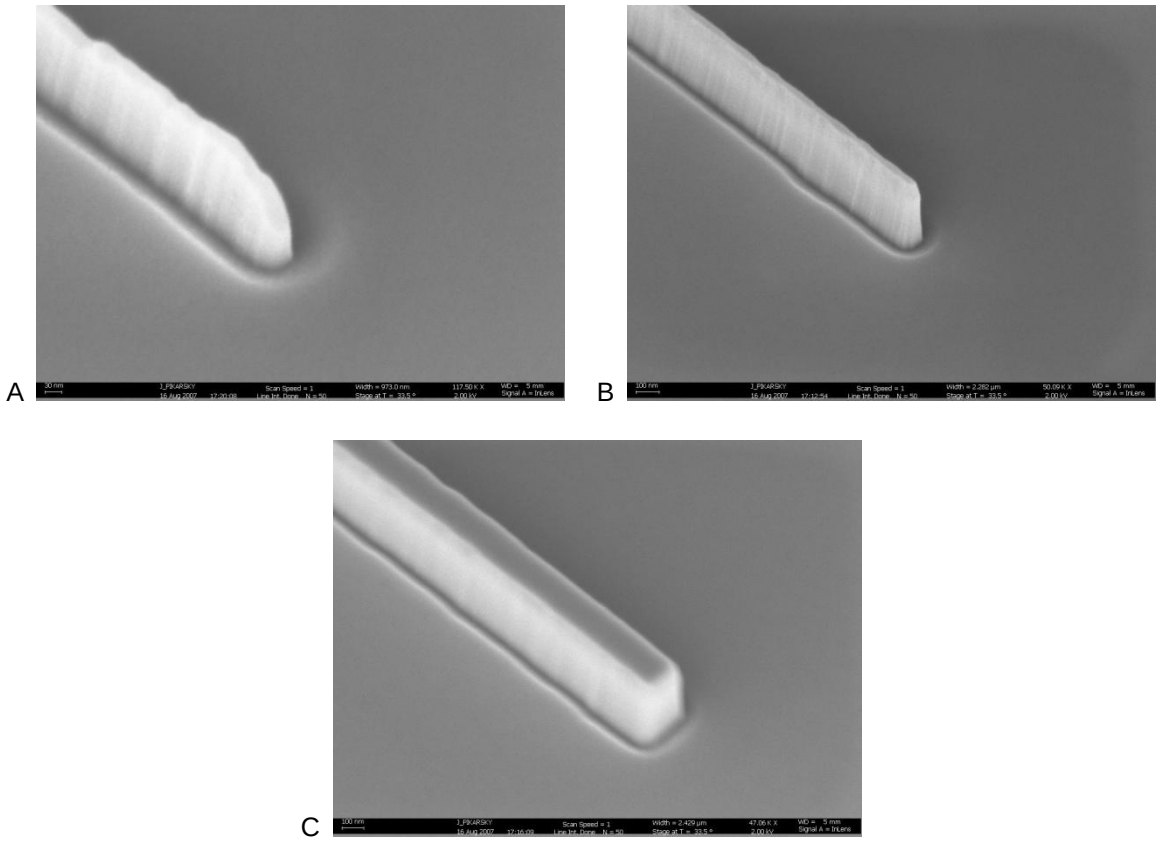

Figure 2.2: Three-quarter views of SiNWs of varying widths

The widths are 15 nm (A), 25 nm (B), and 50 nm (C). Note the decrease in anisotropy at 25 nm and 15 nm and the significant over-etching at 15 nm.

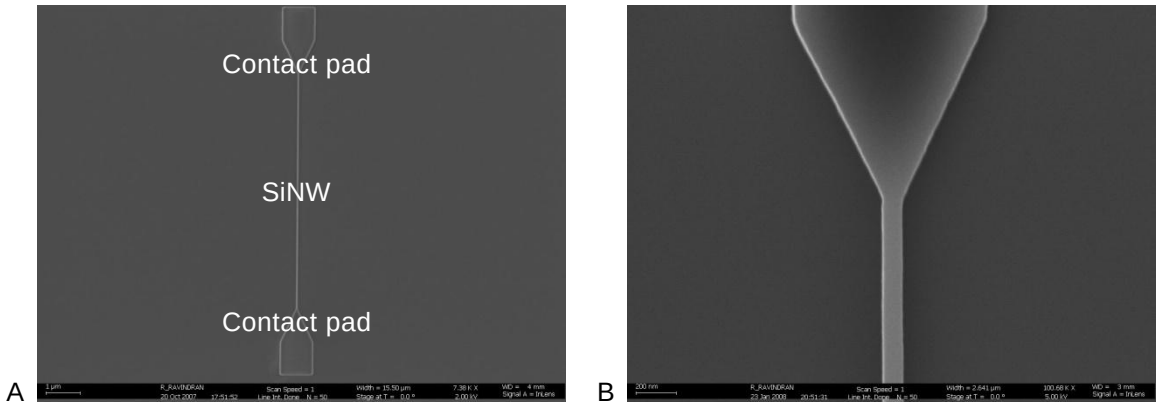

Figure 2.3: Complete SiNW with contact pads for metal electrodes

The wire is 5 μm long and the contact pads are 1 μm wide.

All subsequently described work used a SiNW of the geometry shown in Figure 2.3, but of either longer or shorter channel lengths. A false color SEM in Figure 2.4 highlights this typical SiNW.

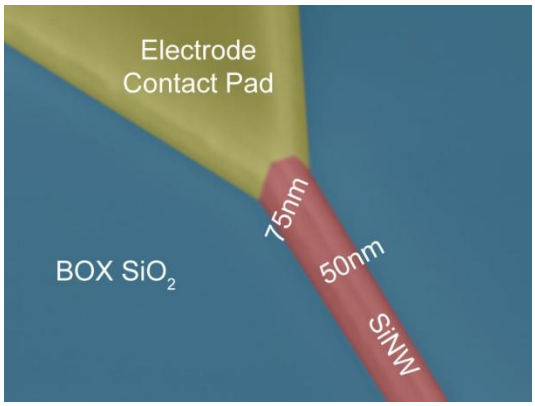

Figure 2.4: Three-quarter view false-color SEM of one end of a SiNW

Multiple electrode configurations were also tested but the high-yield of the SiNWs ultimately enabled the longest test length of 25 μm with a common source electrode to be used. This allowed a large effective sensing area due to the length and more SiNWs to be fabricated in a given area due to the shared source electrode. Optical lithography (Karl Suss MA-6) defined the electrodes. E-beam evaporated (CVC) Ni was initially used for the electrodes because of some promising then-current work on forming low-resistance NiSi alloys. [59] However, poor reliability with Ni, discussed later in this chapter, resulted in a switch to a more conventional choice of e-beam evaporated Al for the electrodes. [27] Following metallization and lift-off, a 400 °C rapid thermal process (RTP), (AET RTP) anneal in forming gas created ohmic contacts between the

electrodes and the SiNWs. Some of the electrode test configurations are shown in Figure 2.5.

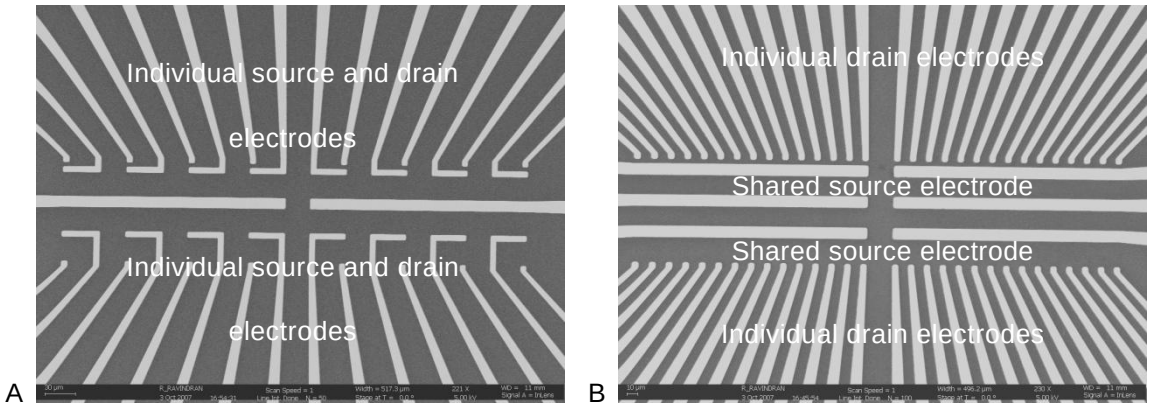

Figure 2.5: Top-down views of two electrode configurations

Configuration (A) has dedicated source and drain electrodes for each SiNW, whereas configuration (B) has a common source "rail" electrode for all SiNWs. Both configurations have two channel lengths of 5 and 25 μm. (B) was the final test configuration used for measurements.

NR9-1500PY photoresist (Futurrex) was initially used to protect the electrodes and form a well for wet measurements. However, this was later switched to SU-8 (Microchem), again for reliability reasons.

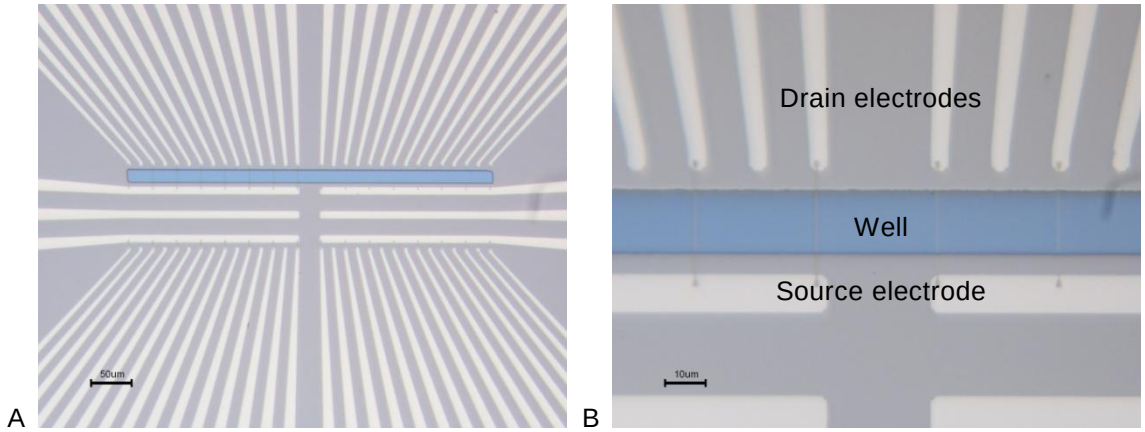

Figure 2.6: Images of a fabricated test chip

The well is 20 x 500 μm.

2.3 Measurement Considerations

There were two primary considerations for electrical measurements. The first choice was between AC or DC measurements and the second choice was in the region of operation. AC sensing measurements almost universally use a lock-in amplifier while DC measurements can be performed with a combination of DC sources and greatly simplified with the source measure units found in semiconductor parameter analyzers. They both generally yield similar performance. [29, 34, 60, 61] DC measurements using parameter analyzers were chosen for this work for a few reasons. First, this is identical to how a FET is characterized and operated. Second, all the biasing including the back-gating could be performed with one unit. Third, additional properties including leakage currents and transconductance could be extracted from one set of data, greatly aiding characterization and troubleshooting of the devices. The basis for selecting DC biasing was therefore determined by both pragmatic and technical considerations.

The choice of the mode of operation or biasing region was purely driven by technical considerations. The carrier screening length in Si, the length at which a single surface charge is screened by the bulk semiconductor, λ_{Si}, is ≈20 nm at the carrier concentrations in the wafers used in this work. [62] In the sub-threshold region, where λ_{Si} is larger than the cross-sectional dimensions of the device, the carrier density is, to first principles, defined by Fermi-Dirac statistics. [61, 62] Thus:

$$n = n_i \cdot e\left(\frac{E_F - E_i}{k_B \cdot T}\right) \tag{2.1}$$

Where E_F is the Fermi level (eV), E_i is the intrinsic Fermi level (eV) and n_i is the intrinsic doping concentration (electrons/cm^3).A change in carrier density is therefore related to a change in surface potential, φ (V), by:

$$\Delta n = n \cdot e\left(\frac{q \cdot \Delta\phi}{k_B \cdot T}\right) \tag{2.2}$$

It then follows that I_D is exponentially proportional to the surface charge: [63]

$$I_D \propto e^{\sigma} \tag{2.3}$$

Ideally, this would imply a great mode of operation for a high-sensitivity sensor – one where linear changes in surface charge result in exponential changes in carrier density and drive current. However, currents in the sub-threshold region are also at least two or three orders of magnitude lower than those in the linear region for most types of charge based sensors, even carbon nanotubes. [64] This in turn places a higher burden measurement apparatus and unfortunately a noise burden that was too high to reliably overcome with the available measurement setup.

There is also an upper bound on our biasing region. In saturation, I_D has a quadratic dependence on surface charge: [63]

$$I_D \propto \sigma^2 \tag{2.4}$$

However, the V_{DS} biasing potentials required for getting into saturation are too large for a biosensor and result in spurious current paths along the surface of the SiNW from the source to drain. [65] In fact, initial devices operated in saturation often failed.

The chosen linear region was the most pragmatic compromise between a sufficiently high I_D, one that is far more reliably measureable, and a low V_{DS}. The surface charge to current relationship here, and as previously described in Chapter 1, is: [63]

$$I_D \propto \sigma \tag{2.5}$$

It is important to note here that in an accumulation mode SiNW sensor, the colloquial definition of threshold voltage is similar to that of an inversion mode FET, but it is physically different. In an inversion mode FET, the threshold voltage is the point at which an inversion channel completely links source and drain and minority carriers become the dominant source of channel conduction. In an accumulation mode SiNW sensor, the threshold voltage is generally considered the point at which the V_G/I_D relationship becomes fully linear as there is no inversion channel. [61, 65-67] The linear region in this definition for an accumulation mode test device is shown in Figure 2.7.

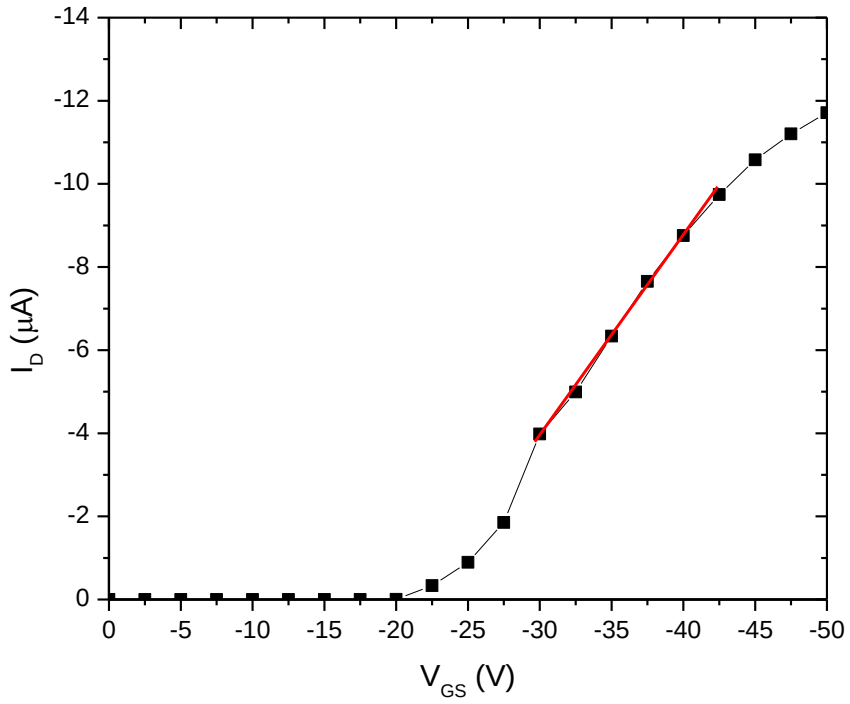

Figure 2.7: The linear region for a process development device

The linear region is indicated by the red line from ≈-30 to -40 V_{GS} at -5 V_{DS}.

2.4 Dry Measurements

All measurements described in this work were performed in a mechanically isolated and electrically shielded Cascade enclosure with a Cascade Alessi/Micromanipulator probestation and probes. The source and drain electrodes were contacted via tungsten probes and the back-gate via the chuck. A HP/Agilent 4156A semiconductor parameter analyzer with four independent source-measure units was used to perform all the measurements. The measurement setups specific to each test are shown in their appropriate chapters.

Source, drain, and gate bias polarity and current direction definitions as used throughout this work are shown in Figure 2.8 and follow conventional FET semantics with the BOX and carrier layer serving as the field oxide and back-gate, respectively, and the SiNW as the channel. [68]

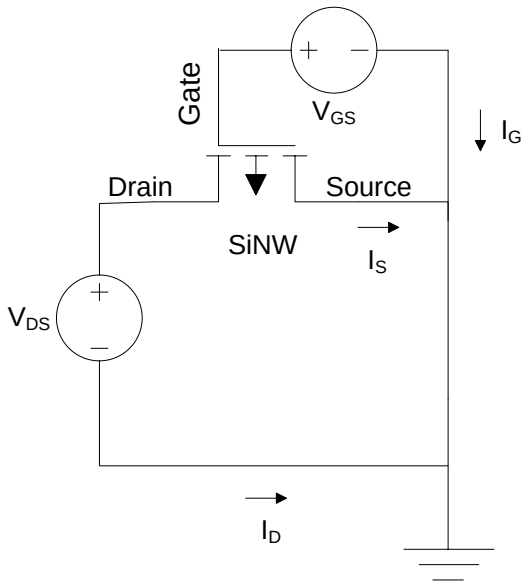

Figure 2.8: General biasing configuration and terminal polarities

A typical set of dry transfer curves for a 25 μm long SiNW test device is shown in Figure 2.9. V_{GS} was swept from 0 to -50 V in increments of -10 V.

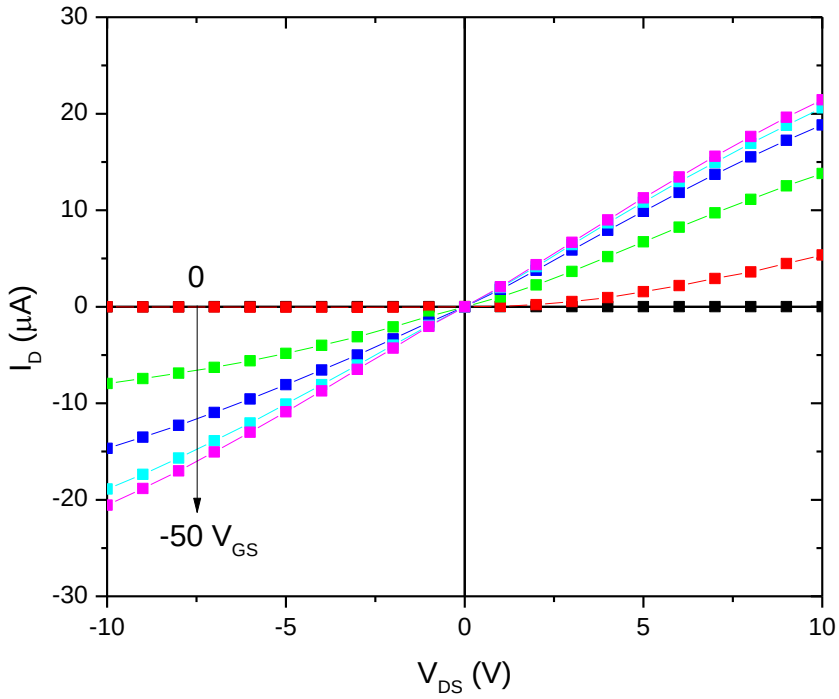

Figure 2.9: Dry IV curves for a process development device

2.5 Wet Measurements

After establishing a satisfactory fabrication workflow and verifying the basic operation of the SiNW devices, attention turned to testing in the PBS ambient that would be applicable for the experiments of Chapters 3-5. Initial wet measurements centered purely on testing the survivability of the devices in pH 7.6 PBS. Samples were manually loaded into cell cloning cylinders (Dow Corning) with a micropipetter as shown in Figure 2.10.

A 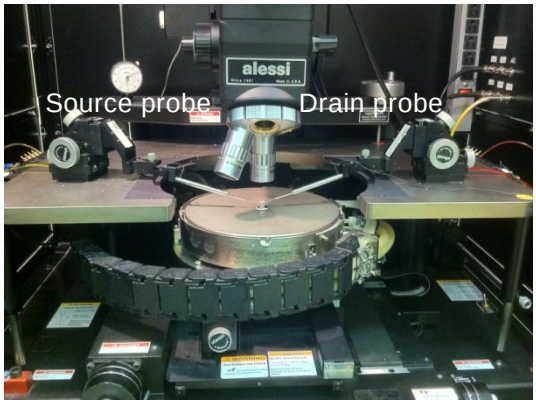

B 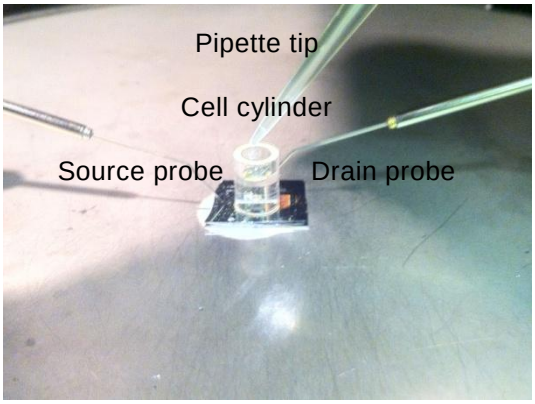

Figure 2.10: Testing setup for preliminary testing

At the beginning, the devices were plagued with extremely poor reliability in PBS. An inspection of the transfer curves and SEM and optical images of failed devices revealed one of two things in these devices. Invariably, the SiNW itself failed leading to an open circuit or the drain shunted to the source. The former case of SiNW failure was the result of large V_{DS} biases in the saturation region in PBS – a driver behind why devices were thereafter operated in the linear region.

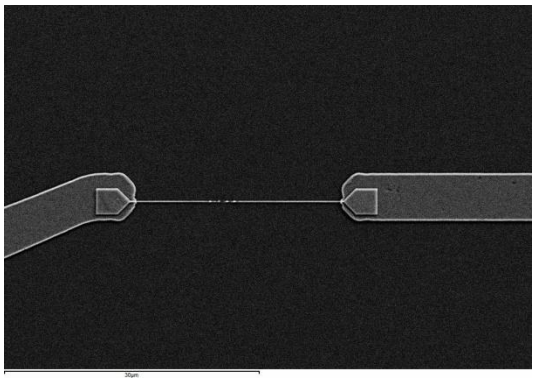

Figure 2.11: Bias induced damage of a SiNW

Note the break in the middle.

The latter case of a drain to source shunt was actually the result of two different and independent causes. The most common cause was inadequate passivation of the electrodes which allowed the solution to penetrate the boundaries of the well. This was resolved with the previously mentioned two-fold solution. First, the electrode metal was changed from Ni to Al and the photoresist defining the wells was changed from the organic polymer based NR9-1500PY to a hard-baked epoxy based SU-8.

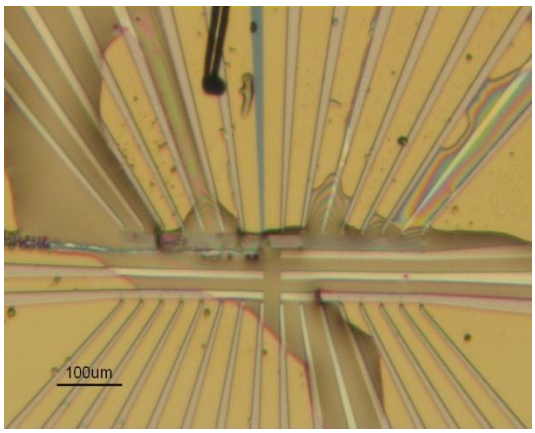

Figure 2.12: Passivation failure in a test device

Note the damage to the common source electrode and the biased center-left drain electrode.

Poor surface passivation of the SiNWs was the other contributor to an undesired current channel between drain and source through the PBS. High-temperature annealing of non-planar FET devices in both O_2 and H_2/N_2 has been shown to improve device performance, primarily by reducing etch induced damage and to also form a thin insulating SiO_2 or SiN layer on the SiNW surface. [69, 70] A two minute 900°C RTP in

O_2 was added after the ICP etch to accomplish both of these functions. The drive current increase is shown in Figure 2.13.

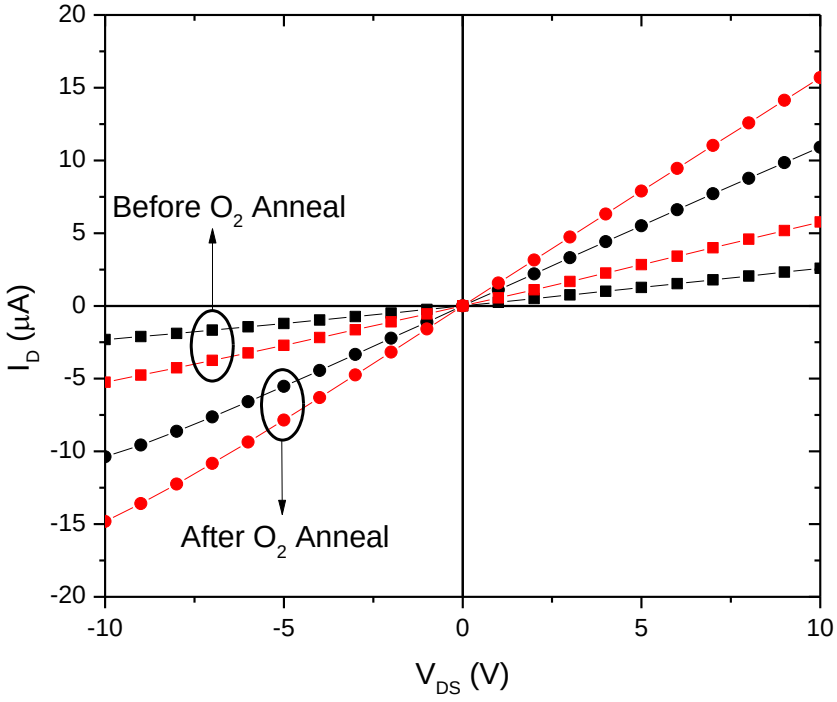

Figure 2.13: Dry IV curves before and after oxygen annealing

The black curves are 50 nm and the red curves are 100 nm SiNWs. V_{GS} was –20 V.

The O_2 anneal also reduced leakage between the SiNW and the solution because of the formation of ≈3 nm of SiO_2 on the SiNW surface, a fact even more relevant for a sensing application. SiNW to solution leakage measurements involved a unique configuration that used an Ag/AgCl electrode held in a well as shown in Figure 2.14. A voltage sweep of V_{DS} with a grounded Ag/AgCl electrode in PBS confirmed the improvement in SiNW passivation as measured by both the hysteresis and leakage current magnitudes, the former of which is often a result of surface states on Si. [71]

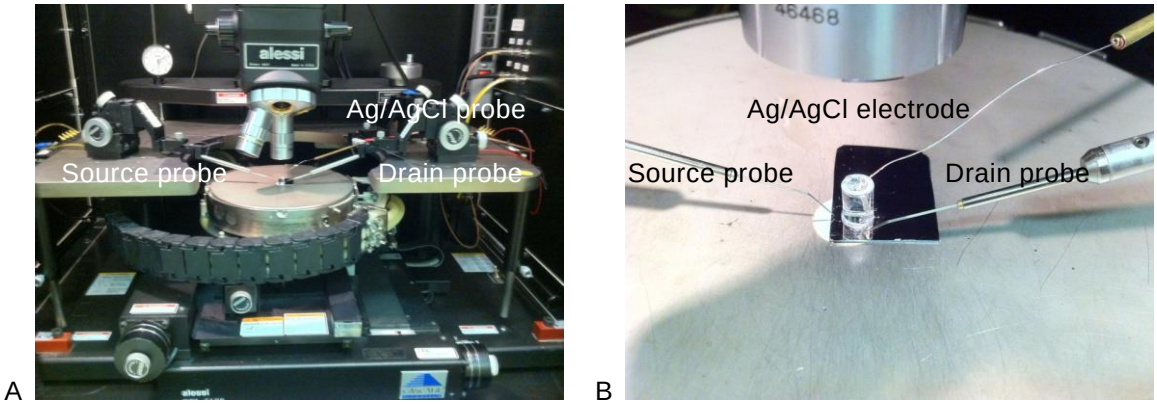

Figure 2.14: Testing setup for leakage testing

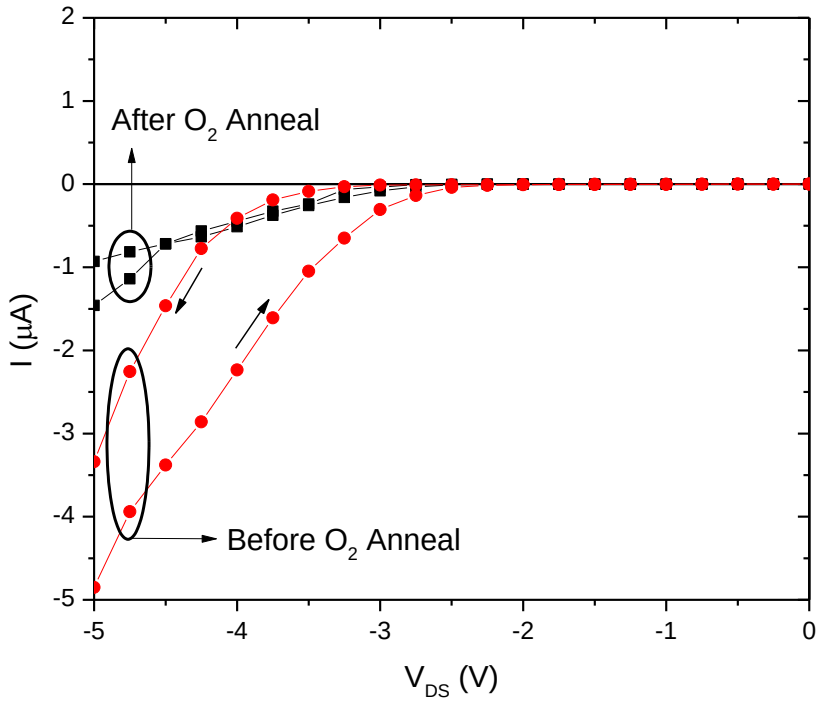

Figure 2.15: SiNW to PBS leakage currents before and after oxygen annealing

V_{GS} was held at 0 V.

Fortuitously, this annealing not only resolved the leakage issues and improved device performance, but also brought the workflow closer in step with non-planar CMOS fabrication. [70] A detailed look at the entire workflow is presented in the Appendix in Table 7.2.

For preliminary device sensing characterization in biologically relevant solutions, a test sensor was first used to perform pH sensing, one of the canonical tests of charge-based sensors. The relative concentration of H^+ and OH^- ions in a buffer solution results in the protonation or deprotonation of the terminal Si–OH groups on the SiNW, thereby altering the surface potential on the SiNW and consequently the channel conductance. [72] PBS at pH values of 2.8, 7.6, and 12.3 was used. Figure 2.16 shows the response of a SiNW sensor to these three buffers Biasing was -5 V_{DS} and -8 V_{GS}.

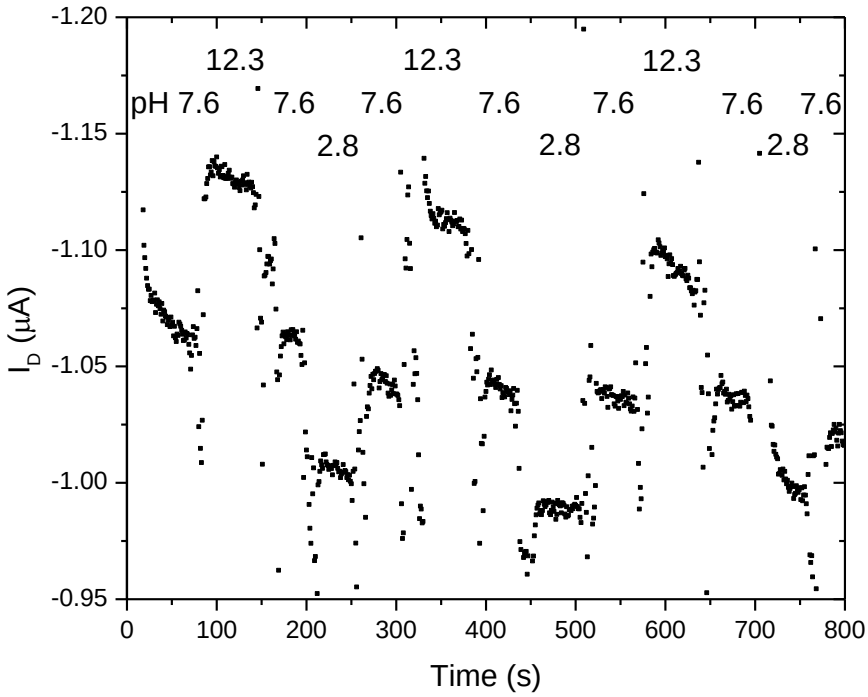

Figure 2.16: Time-dependent response to varying pH solutions

As expected, the more basic pH 12.8 buffer with an abundance of negatively charged OH^- ions increased the magnitude of the drain current. Conversely, the more acidic pH 2.8 buffer with an abundance of positively charged H^+ ions decreased the magnitude of the drain current. The hysteresis is due to the well configuration which required the previous sample to be drawn out before the next one was introduced.

2.6 Summary

This chapter discussed the considerations that went into establishing both fabrication and measurement baselines used in the subsequent work. The electrical measurement setup was defined by technical limitations of the measurement equipment, namely the minimum measureable currents which dictated operation in the linear region. The fabrication workflow was defined by process limitations, performance considerations, and efforts to mitigate device failure. Dry and wet measurements confirmed the ability of these baselines to enable a simple and effective SiNW sensing setup compatible with standard both CMOS fabrication and FET measurements.

3 CELL-LINE SENSING WITH A LOW-DENSITY ARRAY

3.1 Background

While simply using SiNW sensors, or any other label-free scheme in isolation does leverage certain advantages, such as reducing processing steps compared to labeled schemes, there are far more substantial advantages to be had with a chip featuring multiple arrayed sensors fabricated using a workflow that is harmonious with modern, non-planar, IC fabrication methods. [48, 73]

This chapter discusses two main topics. The first is the top-down fabrication of a SiNW array with 16 sensors in isolated polymer wells – an early step towards the electronic microplate. The second is a practical use of this sensor array for a new type of differentiation method between cancerous and non-cancerous ovarian epithelial cell-lines. [74]

3.2 Cell-Line Low-Density Array Fabrication

The SiNW array fabrication process closely followed the baseline process described in Chapter 2. It began with a SOI wafer with a 70 nm thick device layer (p-type, 1-10 Ω-cm), a 145 nm BOX layer, and a 500 μm handle layer. EBL was used to define a 4 x 4 array of 50 nm wide x 70 nm tall x 50 μm long SiNWs per 1 x 1 cm chip. It is important to note that this relatively low density of sensors was chosen not because of any inherent process or design limitations, but to facilitate simple manual sample spotting via micropipettes for the tests reported in this chapter. A flow-through system

was used for the tests reported in Chapters 4 and 5. Chapter 5 goes on to describe how this sensor density was scaled by approximately three orders of magnitude.

Following EBL, the device layer was anisotropically etched down to the BOX using the same Ar/Cl_2 plasma process in an ICP, which in turn formed the SiNWs. The sample then underwent a 900 °C RTP anneal in an O_2 ambient. Optical lithography was then used to define the Al source and drain electrodes which were subsequently deposited using e-beam evaporation. After lift-off, a 450 °C RTP anneal in forming gas created ohmic contacts between the Al electrodes and SiNWs, with the slightly increased temperature producing more reliable contacts. To protect the electrodes and define the wells, two layers of SU-8 epoxy based photoresist were deposited. The first 2 μm thick layer protected the electrodes and opened up 40 x 40 μm windows around the SiNWs and the probing pads while the second 100 μm thick layer formed the 1 mm diameter wells into which the samples were loaded. An overview of this workflow is shown in Figure 3.1 and images of a completed SiNW array in Figure 3.3. Again, a more detailed look at the processing steps is given in the Appendix in Table 7.3.

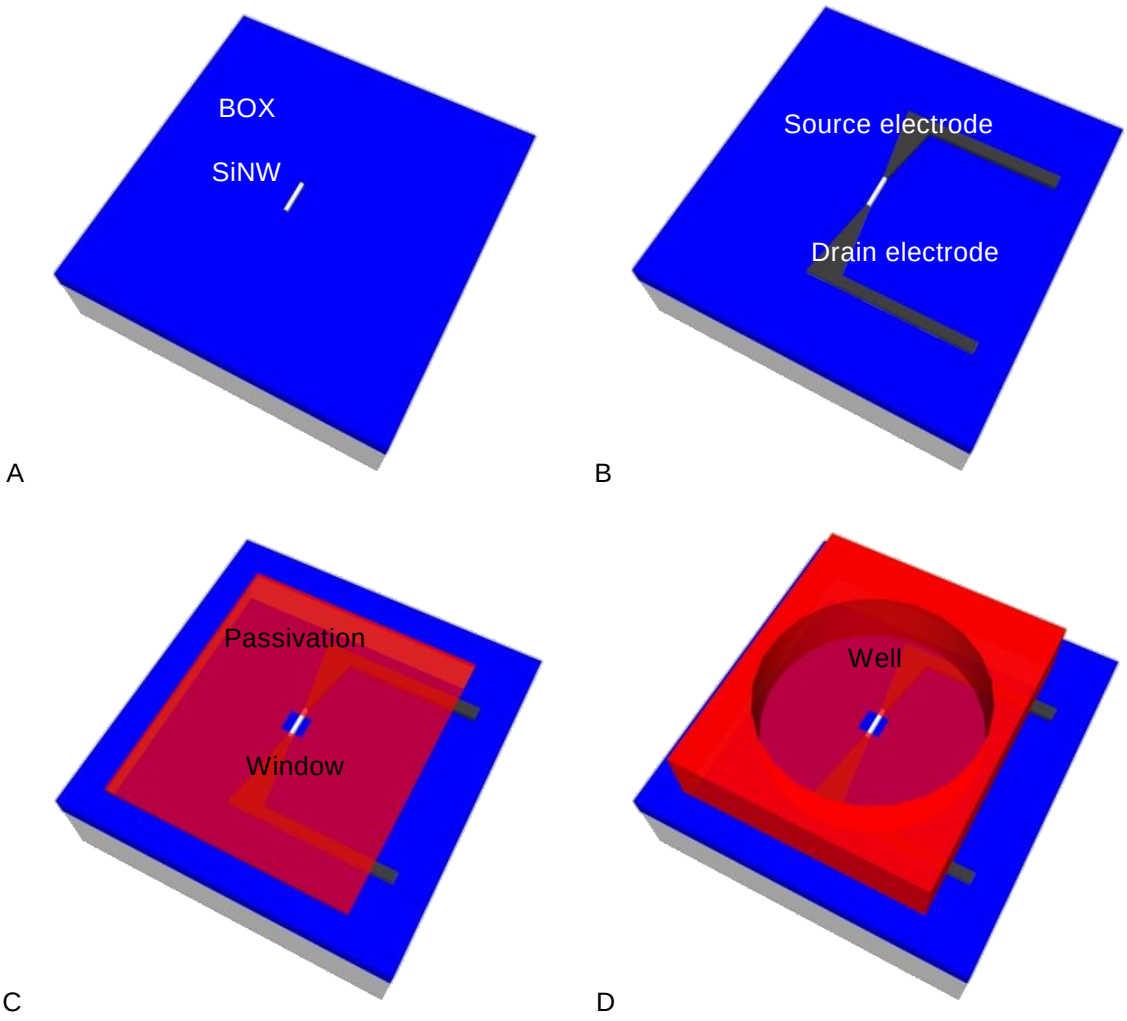

Figure 3.1: Depiction of the low-density array processing workflow

For simplicity, only one well is shown. The SiNW was first defined on the device side of the SOI wafer (A) followed by electrode formation (B). Next, the electrodes were passivated (C), and finally the well was formed (D).

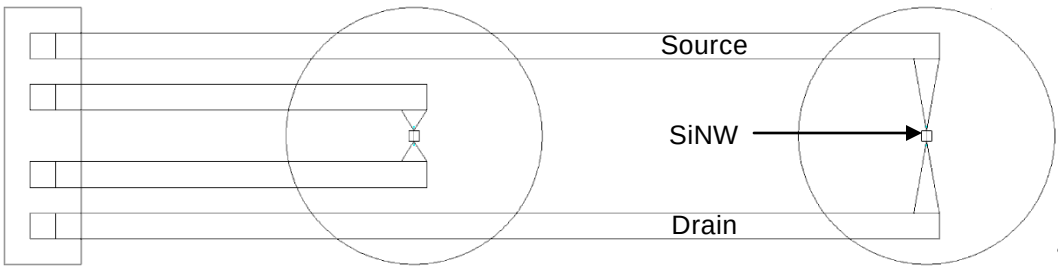

Figure 3.2: CAD layout of a single low density chip

A close-up of two sensors is shown.

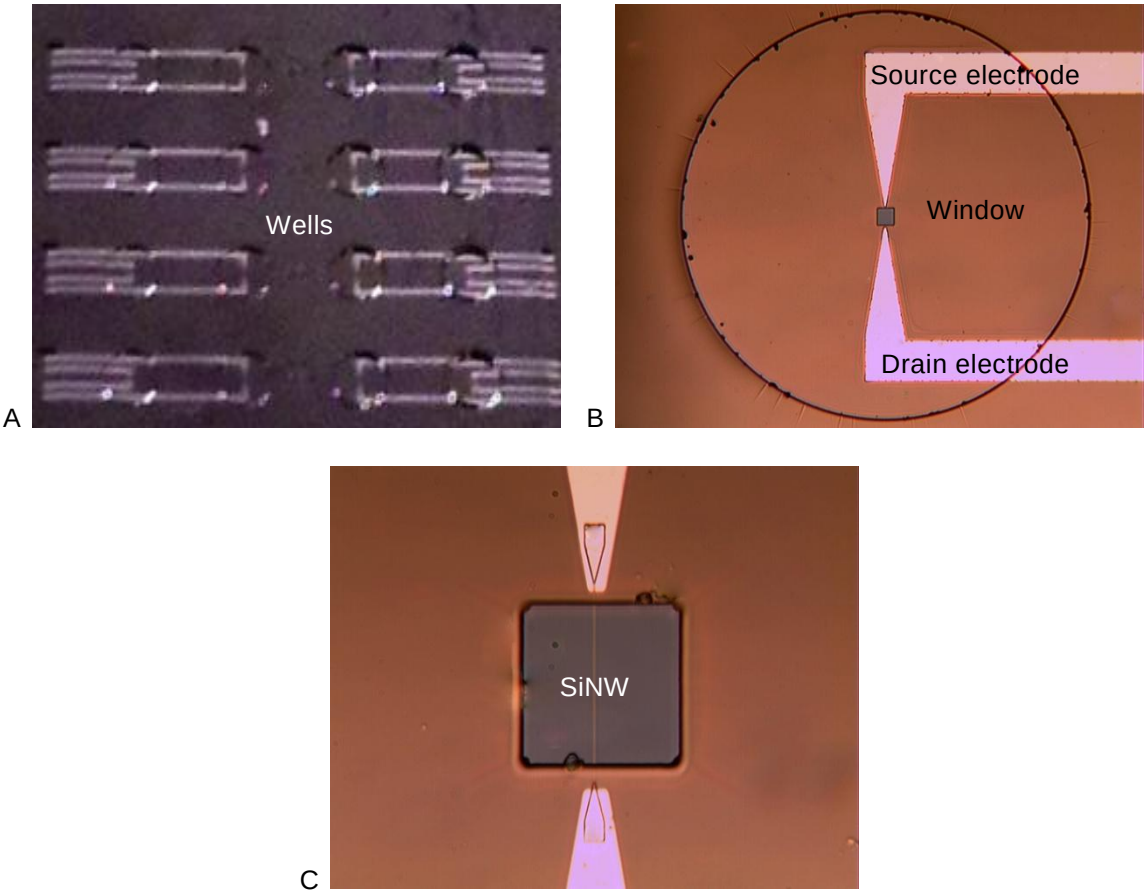

Figure 3.3: Images of a fabricated low-density array chip.

Shown are a 1 x 1 cm, 4 x 4 array (A), an individual 1 mm diameter well (B), and the 40 x 40 μm window revealing the 50 nm x 70 nm x 50 μm SiNW

3.3 Characterization Measurements

The devices were again operated as accumulation mode, back-gated transistors in the linear region. Measurements were made in dry and wet conditions. Standard I_D vs. V_{DS} curves from initial dry measurements are shown in Figure 3.4.

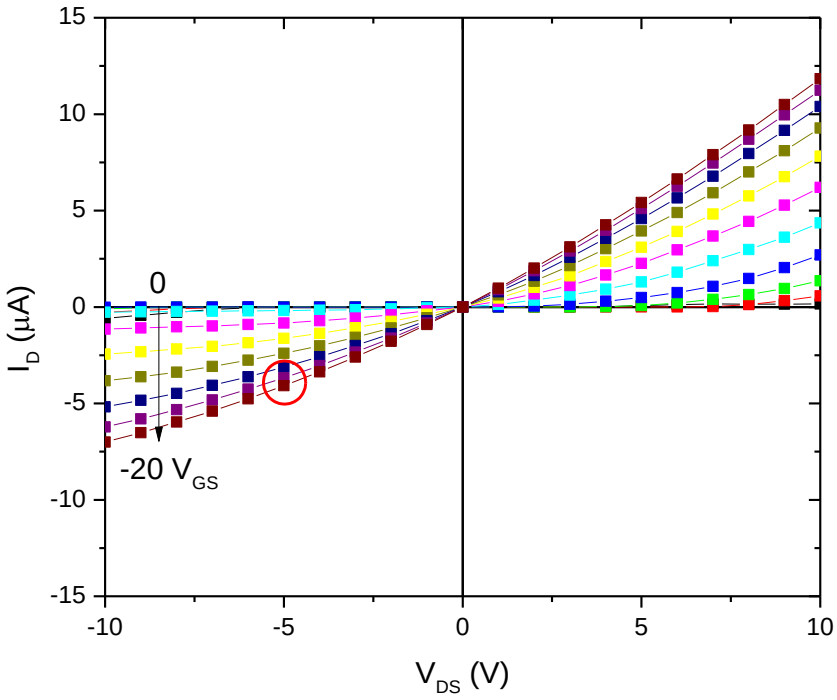

Figure 3.4: Dry IV curves for a low-density array

The red circle indicates the -5 V_{DS} biasing point used in sensing experiments.

Figure 3.5 shows the average and ± two standard deviation I_D for all 16 sensors in one array. The sensors actually used for the sensing experiments fell within even tighter tolerances, less than ± 5 %, of each other.

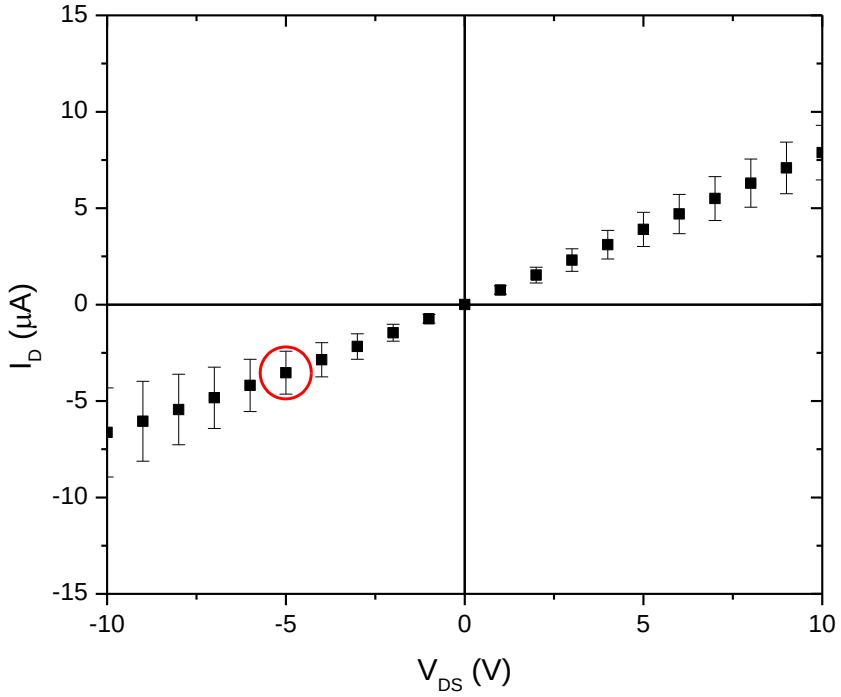

Figure 3.5: Average and ± two standard deviation I_D for 16 sensors in an array

Again, the red circle indicates the -5 V biasing point used in sensing experiments.

Next began wet measurements and characterization. I_D vs. V_{GS} curves were first measured. These curves were then used to determine the peak transconductance point in the linear region at V_{DS} = -5 V and that biasing point was then used for all wet sensing measurements. In all subsequent discussions, the standard definition of transconductance, g_m, is used and calculated internally by the measurement tool:

$$g_m = \frac{\Delta I_D}{\Delta V_{GS}} \tag{3.1}$$

The peak back-gated g_m in pH 7.6 PBS was typically around 0.2 μS and occurs near V_{GS} = -20 V. Typical I_D and g_m vs. V_{GS} curves are shown in Figure 3.6.

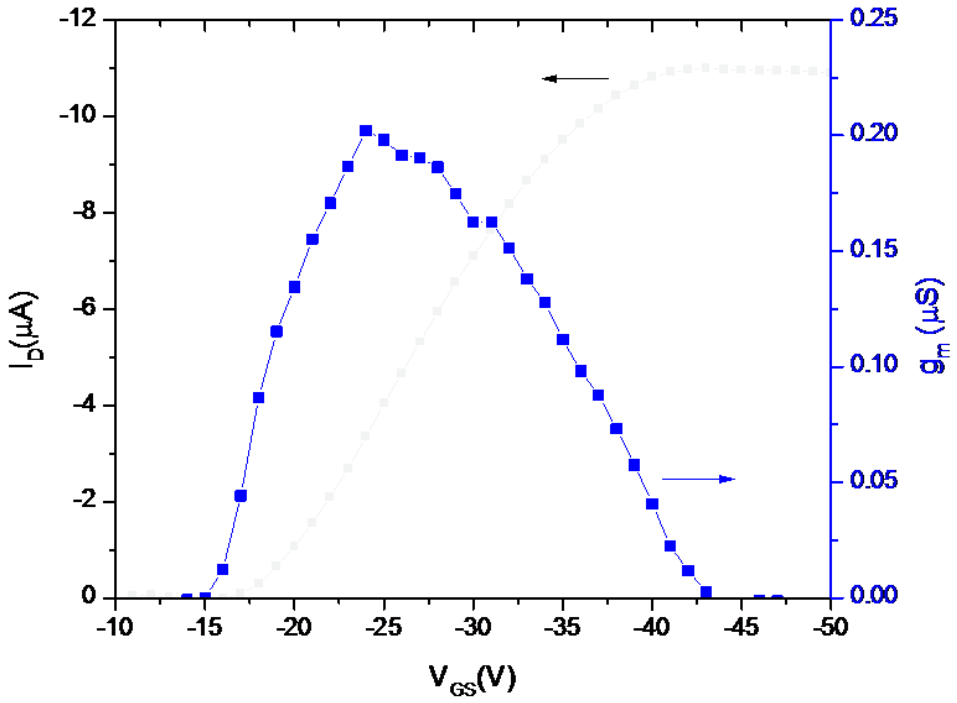

Figure 3.6: Wet I_D and g_m vs. V_{GS} curves in pH 7.6 PBS for a low-density array

There are two noteworthy points to be made about wet measurements. The first is that gate biasing was provided by the back-gate during transconductance measurements, and therefore would only be expected to be an approximate indication of the optimal gate bias for biochemical sensing, which occurs as the result of surface charge changes on the sides and top of the SiNW. However, previous work has shown back-gate biased transconductance to be an effective gauge of sensing performance. The second is a roughly factor of two reduction in I_D in PBS compared to the dry conditions. The same previous work has indicated that this reduction is the result of a PBS/SiO_2 equilibrium resulting in a net positive change in surface charge. Both points are discussed in greater detail in the prior work. [65]

3.4 Arrayed Cell-Line Sensing

The first of the two new applications for a label-free sensor discussed here is the differentiation of two cell lines. The second application, detection of paramagnetic particles, is discussed in Chapter 4.

While pH sensing was initially used to test the fabrication process and the measurement setup in the development stages, the ultimate objective of the low-density sensor array was not to recreate a pH meter. Rather, the objective of the low-density array was to develop new biological sensing applications for a SiNW sensor. To this end, a new method for differentiating between two human ovarian cell lines was developed that fundamentally differs from prior methods that have traditionally relied on genetics or proteomics for differentiation. [75-77] The first of these cell lines, immortalized ovarian surface epithelial (IOSE), was an immortalized cell line that consisted of healthy epithelial ovarian cells. The second, human ovarian carcinoma (HEY), was a cell line that consisted of cancerous epithelial ovarian cells. Working under the hypothesis that the contents and makeup of the two cell lines should differ due to the more aggressive proliferation demands of the cancerous HEY cells, samples were made containing the contents of these cells at specific concentrations.

Because sensing was of the intracellular contents which do not bind directly to any receptor on the surface of the SiNWs, a large Debye length was preferred. [39] This is quite similar to the detection of ions in solution with SiNW sensors. [26, 78] Following from the discussion in Chapter 1 and using Equation 1.8, 1x PBS has a λ_D of 0.7 nm, 0.1x PBS of 2.3 nm, and 0.01x PBS of 7.3 nm. The large screening length of 0.01x PBS was chosen for these measurements to maximize the effects of the charges in solution.

For the tests in this chapter, a micropipette was used to both introduce and withdraw ≈10 μL of solution in to and out of the hydrophobic SU-8 wells. The micropipette tips were changed between solutions. The testing setup is shown in Figure 3.7. Also, the t = 0 s point started after ≈100 s after pH 7.6 PBS had first been introduced into the well to allow stabilization of I_D.

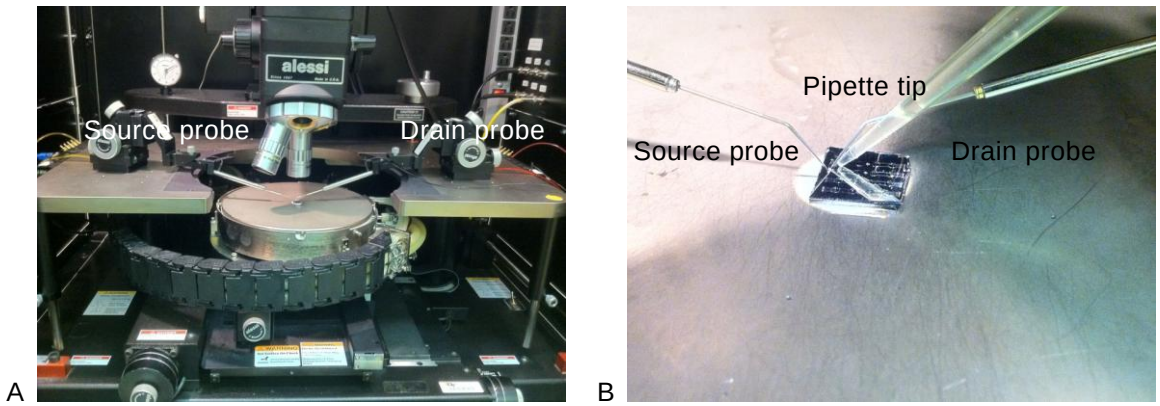

Figure 3.7: Testing setup for arrayed cell line sensing

At the highest concentration, two samples were made, each with the contents of 750,000 cells from either the IOSE or HEY cell lines per 1 mL of pH 7.6 PBS. These two samples were then serially diluted into concentrations of 75,000 cells/mL PBS and 7,500 cells/mL PBS.

Five sensors from a single 4 x 4 array were then used to run identical tests. The tests consisted of switching between the HEY and IOSE samples at all three concentrations. Each sample was left on the chip for approximately 100 s. A time-dependent plot from one of these five tests is shown in Figure 3.8.

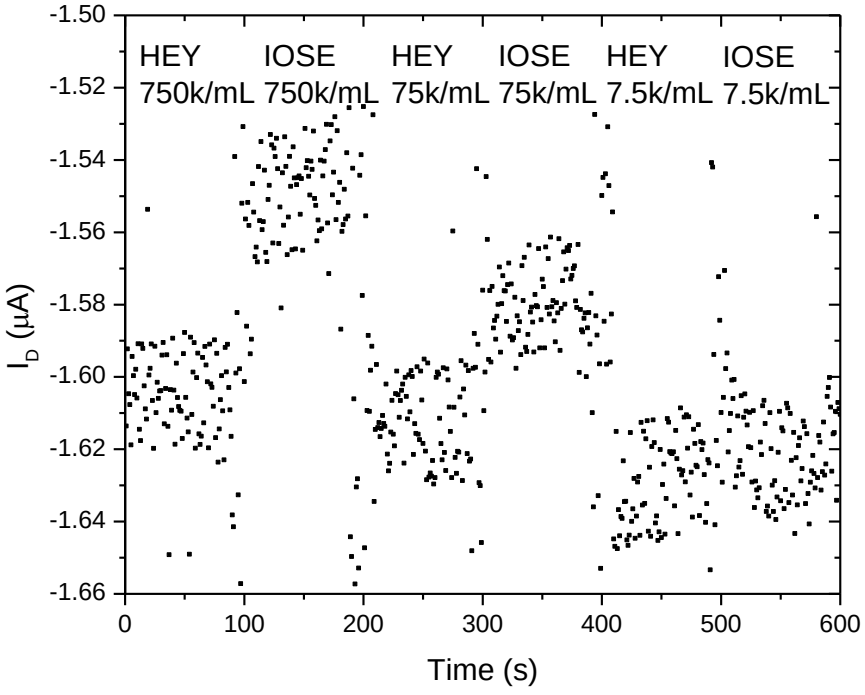

Figure 3.8: Time-dependent response to HEY and IOSE solutions

The solutions were introduced, alternating between HEY and IOSE, and progressively from 750,000 cells/mL down to 7,500 cells/mL. The quantitative change in I_D for these five sensors is shown in Figure 3.9 as the percentage change in I_D between the two cell lines.

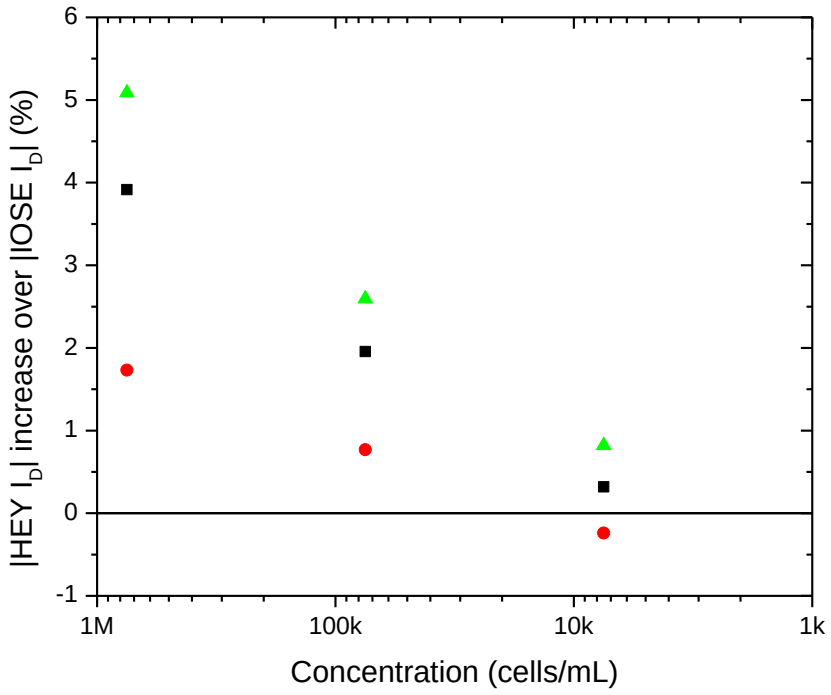

Figure 3.9: Percentage difference in I_D between HEY and IOSE

The black squares are the mean, the red circles the minimum, and the green triangles the maximum change in I_D for the five sensors on a single low-density array at each of the three concentrations.

A number of observations can be made from these tests. The I_D magnitude is greater for the HEY sample than it is for the IOSE sample. The pH values of the samples' buffer solutions were identical. Thus, the change in current does not occur because of the protonation or deprotonation of the $Si\text{-}O^-/Si\text{-}OH$ groups on the SiNW field oxide as was the case in the previous pH tests. The HEY sample must therefore contain more negative charge (or less positive charge) than the IOSE sample because of the larger HEY I_D magnitude. The most plausible explanation is the difference in the

intracellular ion concentrations between the two cell lines. This is supported by the fact that a number of positively charged metal ions (namely Mn^{n+} and Fe^{n+}) have been reported to be found in substantially lower concentrations (a factor of 24 and 4 respectively) in cancerous cells as compared to their healthy equivalents. [53, 79]

Rewriting Equation 1.7 in terms of surface charge density yields:

$$\sigma = \frac{\Delta I_{drift} \cdot n_o \cdot q \cdot h \cdot w}{I_{drift} \cdot 2 \cdot (h + w)} \tag{3.2}$$

Solving this equation for a 50 x 75 nm SiNW with a doping density of $2 \cdot 10^{15}$ holes/cm^3, the following mean changes in surface charge densities are obtained:

Table 3.1: Change in surface charge density

cells/mL	Δσ (statC/cm^2)
750,000	$5.62 \cdot 10^{-2}$
75,000	$2.88 \cdot 10^{-2}$
7,500	$3.60 \cdot 10^{-3}$

With a 7.3 nm screening length, the changes in volume charge density approximate to:

Table 3.2: Change in volume charge density

cells/mL	Δσ (statC/cm^3)
750,000	$7.70 \cdot 10^{4}$
75,000	$3.95 \cdot 10^{4}$
7,500	$4.93 \cdot 10^{3}$

This data offers a unique measurement showing the difference in effective volume charge between two cell lines. Using a concentration of 7,500 cells/mL (where self-screening would be minimal) the change in charge associated with an individual cell

is 0.658 statC/cell, which in turn amounts to a change of $1.37 \cdot 10^9$ units of elementary charge between the intracellular contents of a HEY and IOSE cell. This presents an interesting reference point for future work as no previous comparative data exists.

Since the ions in the HEY and IOSE solutions are also not expected to directly protonate or deprotonate the $Si\text{-}O^-/Si\text{-}OH$ surface groups on the SiNW and the PBS can be expected to maintain a constant proton concentration. The modulation, therefore, arises simply from the close proximity of ionic charges in the solution to the conducting channel in the SiNW. [78] Some indications of this are that the signal to noise ratio (defined as μ/σ) is roughly three times higher for the cancer cell tests than the pH tests and there is very little hysteresis between sample exchanges, even with a manual spotting setup, indicating there are no actual binding/unbinding events at the SiNW surface.

To confirm the statistical significance of the difference between the HEY and IOSE current values, a two-tailed, unpaired t-test is performed on all the tests to obtain the associated p-values. To avoid noise associated with the sample exchanges, only I_D values from the middle 50 s for each sample are used. From this data, it can be concluded that down to a concentration of 75,000 cells/mL, all five sensors yielded statistically significant ($p < 0.05$) results. Table 3.3 lists the resulting p-values.

Table 3.3: p-values of HEY versus IOSE

	Sensor				
cells/mL	1	2	3	4	5
750,000	< .001	< .001	< .001	< .001	< .001
75,000	< .001	< .001	< .001	< .001	< .001
7,500	0.216	< .001	0.059	0.021	0.010

Interestingly, in Figure 3.9, there is a log-linear relationship between the cell concentration and change in current. Such log-linear behavior has been previously reported for SiNW sensing of several molecules and ions ranging from purified cancer markers like prostate specific antigen to pH measurements. [80, 81] More quantitative treatments have attributed this to increased partial screening between the species themselves in solution; that is, an increased concentration of species, be they ions or macromolecules, will partially offset the increased charge resulting from that increased concentration. [37, 38]

3.5 Summary

This chapter discussed the development of a top-down fabricated SiNW sensor array with wells that could be individually spotted and a new application for a charge based sensor. It was also demonstrated that cancerous and healthy ovarian epithelial cells could be differentiated purely based on a difference in charge between their intracellular contents and that this difference was statistically significant at the concentrations tested across multiple sensors on an array.

4 SPION SENSING WITH A LOW-DENSITY ARRAY

4.1 Background

An exciting recent development in cancer research has been the use of superparamagnetic iron-oxide nanoparticles (SPIONs) for the capture of circulating cancerous cells, both as a diagnostic and therapeutic tool. However, here again, sensing capture events resort to labeled methods. This presents another application for a SiNW sensor array, this time to detect circulating functionalized SPIONs.

This chapter discusses one primary topic. A SiNW sensor used to detect circulating superparamagnetic particles functionalized with biomolecules in the presence of an electromagnetic field.

4.2 SPION Low-Density Array Fabrication

The fabrication process and the resulting array were identical to the one described in Chapter 3. Demonstrated robustness of the process and the resulting devices was the key factor in reusing this array.

4.3 Superparamagnetism

Magnetic materials fall into a few general categories, of which two are of note here. Ferromagnetic materials have a permanent magnetic moment and therefore produce a permanent magnetic field. Paramagnetic materials on the other hand only achieve a net magnetic moment in the presence of an externally applied magnetic field. In the special case of superparamagnetism, particles at sufficiently small sizes can form a

single and coherent magnetic domain – unlike ferromagnetism and conventional paramagnetism where there is only a net difference in electron spins. This leads superparamagnetic particles to be strongly influenced in the presence of magnetic fields, but to also become non-magnetic in the absence of magnetic fields. [82] This property has already been leveraged in medicine, particularly in magnetic resonance imaging and for the extraction of tagged tumor both in vitro and in vivo cells, but has not been previously used for direct sensing. [54, 83]

4.4 Functionalized SPION Sensing

The particles used in this work were Fe_3O_4. A depiction of such particles in one of the most basic functionalization schemes with amine and carboxyl groups is shown in Figure 4.1 as a conceptual analogy to the amino acids in Figure 1.3 – actual testing was performed with a protein functionalization.

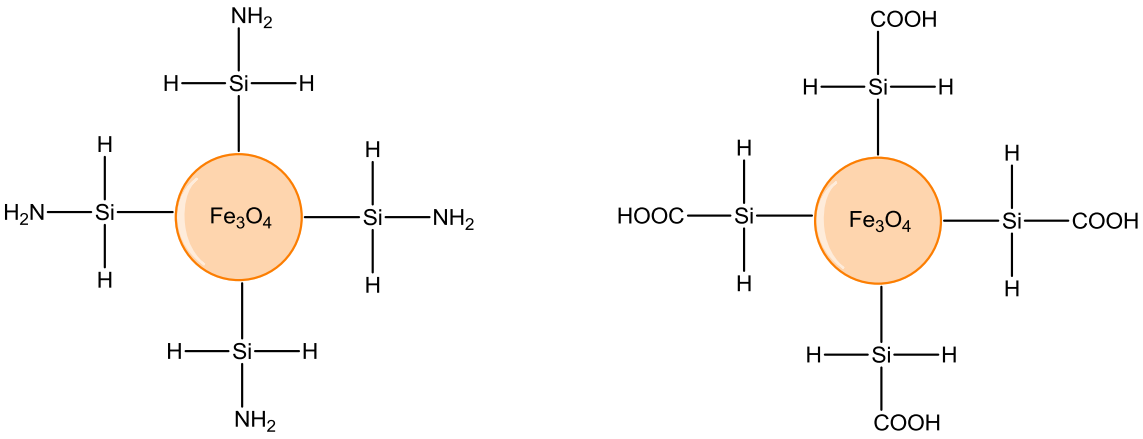

Figure 4.1: Amine and carboxyl functionalized SPIONs

For this test, 1x PBS at pH 7.6 with a λ_D of 0.7 nm was chosen to best mitigate the effects of any SPIONs in solution not actually attracted to the sensor surface by the magnetic field. The starting point was a solution of SPIONs 1 μm in diameter and functionalized with *strepomyces acdinii* bacteria derived strepavidin in PBS (Sigma-Aldrich) at a concentration of 1.0 mg/mL. This solution was then serially diluted into concentrations of 0.1 and 0.01 mg/mL. Strepavidin is a negatively charged protein at a pH of 7.6. [29]

The flow-through setup used a small reservoir, tubing (Tygon), and a peristaltic pump (VWR) operating at a flow rate of 10 mL/min, quite similar to the setups used for the extraction of circulating tumor cells in therapeutic applications. [54] The inlet and outlet tubing entered a 2 mm diameter x 4 mm tall cell cloning cylinder which was capped and sealed with mounting adhesive (Crystalbond).

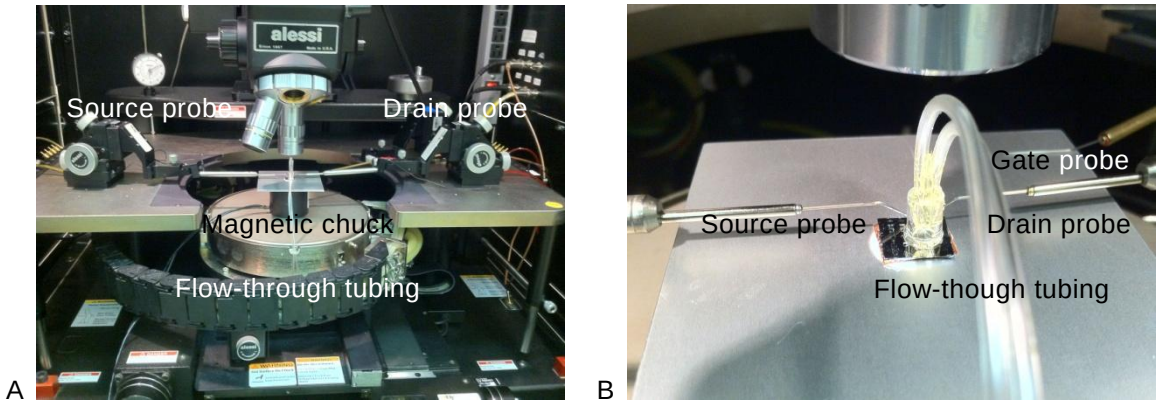

Figure 4.2: Testing setup for SPION sensing

The magnetic chuck is simply a coaxial electromagnet with an Al plate affixed on top. As the vacuum and biasing of the probestation chuck could not be used, double-sided Cu

tape was used to secure the sample. The electromagnet displayed effectively no hysteresis at the testing sampling time of 1 s.

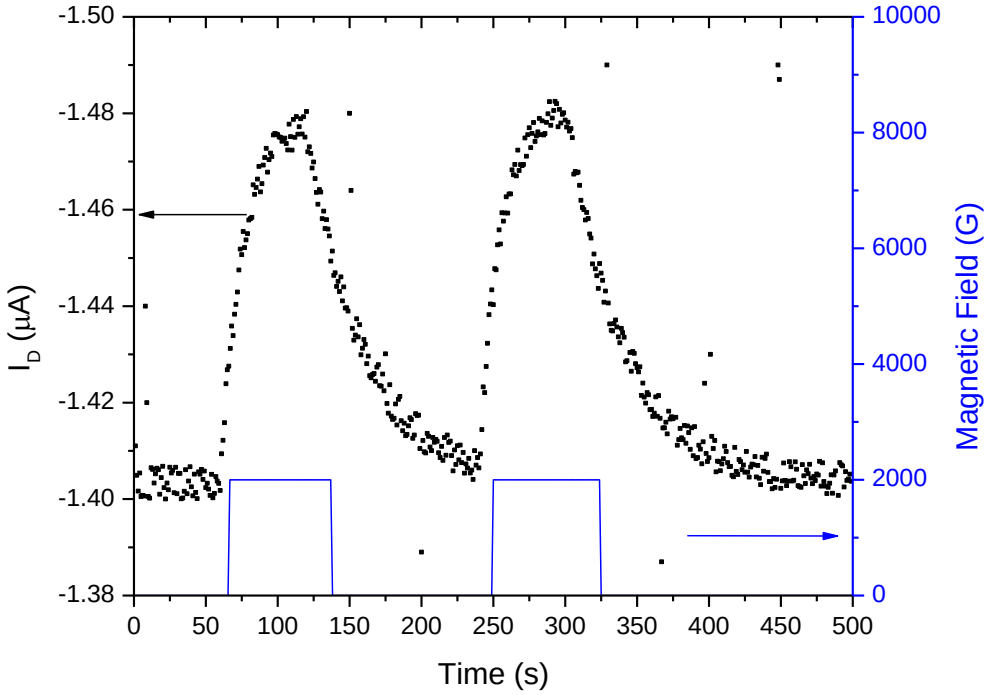

Figure 4.3: Time dependent response for a 1 mg/mL SPION solution

The electromagnet was switched on and off manually, so the plotted timing of the magnetic field is only approximate.

The flow-through configuration combined with the SPIONs only being detected by charge proximity to the SiNW and not by an actual interaction with the SiO_2 surface groups allowed for lower hysteresis during solution exchanges than the configuration of Chapter 2 used for pH measurements. Interestingly, there is actually more noise when the magnet is off. A plausible explanation is that when the magnet is on, the SPIONs are actively held at the sensor surface, whereas with the magnet off, there is likely influence

from the SPIONs merely flowing through near the sensor surface below the short, but non-negligible, screening length, as is the case with the sensing of other biomolecules. [39]

To verify that the electromagnetic fields themselves were not resulting in the change in I_D through any number of mechanisms such as Eddy currents or the Hall effect, however unlikely, a test was performed with just the PBS solution cycled through, but with the electromagnet switched on and off as before. The result validated that the change in current does in fact arise from the magnetic field-induced capture of the SPIONs as per Figure 4.4.

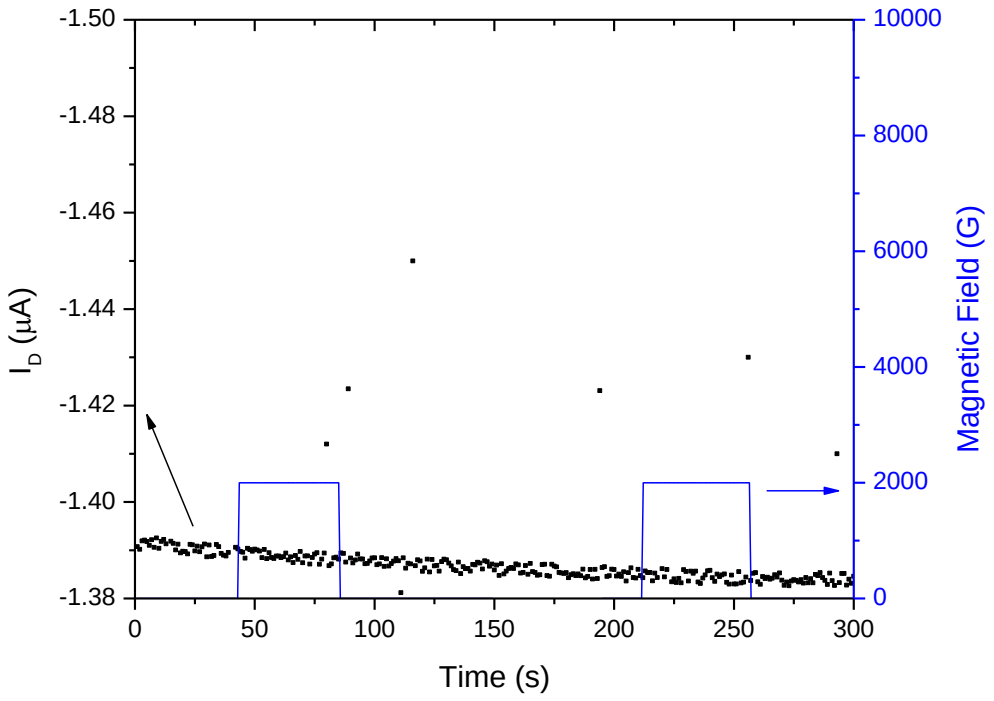

Figure 4.4: Time dependent response for a control solution without SPIONs

The electromagnet was again switched on and off manually, so the plotted timing of the magnetic field is only approximate.

An associated time constant, τ, can be extrapolated from a fit that describes the rise of I_D over time – quite similar to the RC time constant in a passive electronic circuit:

$$I_D(t) = I_{D,max} \cdot e(1 - \frac{-t}{\tau}) \tag{4.1}$$

The extrapolated time constants for three different SPION concentrations of 1, 0.1, and 0.01 mg/mL for three separate tests each are shown in Figure 4.5.

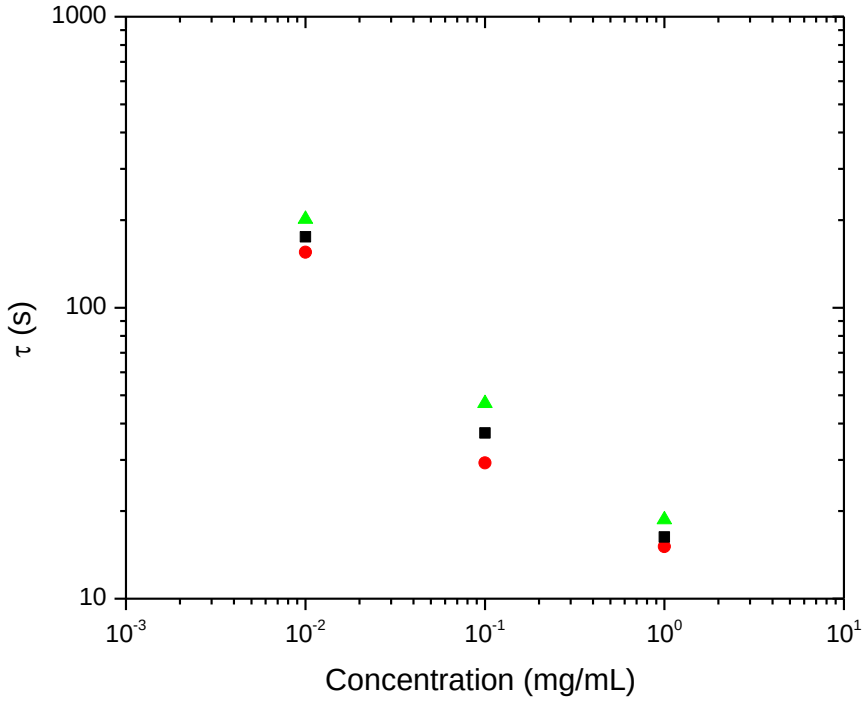

Figure 4.5: Relationship of the rising time constant with SPION concentration

The black square, red circle, and green triangle are three different devices on a single low-density array.

At a flow rate of 10 mL/min (or 0.167 mL/s) and an effective cell cloning cylinder volume of 0.006 mL (approximately one-half of the cloning cylinder due to the

space occupied by the inlet and outlet tubes) an amount of solution equal to the volume of the chamber cycled through roughly 28 times a second. As would be intuitively expected, the time constants have a roughly linear relationship with the SPION concentration. With fewer SPIONs flowing through at a constant solution flow rate, fewer would be expected to be attracted to the sensor surface per unit time as the concentration decreases.

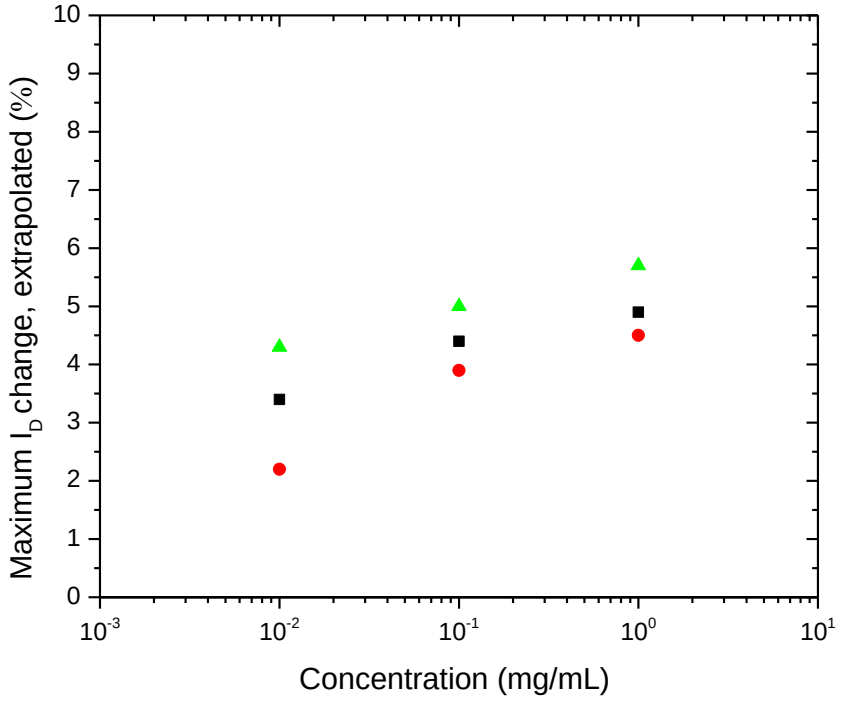

Figure 4.6: Relationship of the extrapolated I_D change with SPION concentration
The black square, red circle, and green triangle are three different devices.

Interestingly, the extrapolated maximum I_D values only vary linearly over three orders of magnitude change in SPION concentration. While perhaps initially surprising, it is easily explained by considering that the electromagnet ultimately only attracts the

SPIONs in solution towards the SiNW and given sufficient time would attract enough SPIONs within the Debye screening length to modulate the current similarly, despite large changes in concentration. As both the time constant and change in I_D versus concentration data represent a new type of measurement and follow intuition, they are similar to the volume charge density results of Chapter 3 and should be considered initial reference points for future tests.

4.5 Summary

This chapter discussed the use of an electromagnet to selectively capture and sense functionalized SPIONs in a manner quite similar to that previously used to capture, but not sense, circulating cancerous cells. Data derived from the wet measurements offered insight into both the capture and sensing processes relevant to flow-through systems.

5 BIOCHEMICAL SENSING WITH A HIGH-DENSITY ARRAY

5.1 Background

Despite the clear merits of a scalable sensing platform and the potential of SiNW sensors to provide just that, there have previously only been scattershot efforts towards truly scaling a completely top-down fabricated SiNW sensor array – incidentally, even most of these have been in the area of photoelectronics and charge storage, not biosensing. [84-86]

This chapter discusses two primary topics. The first is the development of a new fabrication process that uses elements of 3DS, namely TSVs, to develop an indefinitely scalable SiNW high-density sensor array with 10,000 sensors/cm^2 – another key step towards the realization of the electronic microplate. This is a spiritual extension to a different field of the 3DS work performed for stacking memory and logic chips. [87, 88] The second is the dry and wet characterization of this sensor array.

5.2 High-Density Array Fabrication

The fabrication process was a highly scaled combination of two previously discussed methods. The first was the top-down fabricated SiNW array described in Chapter 3 and the second was a new TSV fabrication and plating process. [49, 74] The process began with the same SOI wafer with the 70 nm device layer (p-type, 1-10 Ω-cm) and 144 nm BOX layer as before, but with a thinned 200 μm handle layer to facilitate the incorporation of TSVs at high aspect ratios with the processing tools used. The device layer face is hereafter referred to as the topside and the handle layer face as the backside.

A 2 μm plasma-enhanced chemical vapor deposition (PECVD), (Unaxis) SiO_2 layer, the "mesh" oxide, was deposited on the topside which, in subsequent steps, served as the substrate for the mesh and isolating "islands" and also protected the device layer during the early processing steps. 40 μm TSVs, which ultimately functioned as the source and drain electrodes, were patterned on the handle layer and then etched using an ICP from the backside through the handle, buried oxide, and device layers, stopping at the mesh oxide. The sidewalls of the TSVs were passivated from the backside with a 2 μm PECVD SiO_2 layer. 50 μm diameter islands of the mesh oxide centered on the 40 μm TSVs were then defined with buffered oxide etchant. This exposed the device layer everywhere except around the TSVs. EBL was then used to pattern 25 μm long by 50 nm wide SiNWs at a pitch of 100 μm (10,000/cm^2), which were then anisotropically etched with an ICP as in prior discussions. This was followed by a 900°C RTP in O_2 which again had the same function as before. The meshes, a grid pattern of holes in the mesh oxide centered on the TSVs, which served as the starting point for electroplating, were then etched with a reactive ion etch (RIE), (Vision Oxide).

A multi-step electroplating processing was then utilized. Au was first deposited on top of photoresist, which in turn was on top of the device layer. The Au offered a chemically inert electrical contact with the mesh patterns on the TSVs during electroplating while the photoresist underneath allowed for a simple lift-off process to remove the Au after electroplating without damage to the Cu TSVs, or the Si and SiO_2. The mesh was first "pinched-off" from the topside in a Cu electroplating solution to form an electrical constant from the Au to the TSVs and the TSV was fully plated

through from the backside. The Au was finally removed using lift-off – this approach eliminated the need to use metal etchants to selectively remove the Au.

Al electrodes connecting the TSVs with the SiNWs were defined on the topside. A 400°C RTP (lower than the 450 °C used previously in the low-density array to minimize any effects of variances in the coefficient of thermal expansion between the Cu TSVs and Si/SiO_2) in forming gas formed ohmic contacts between the Al electrodes and SiNWs. [89] As a result of this consideration, there were no issues resulting from the expansion mismatch between the Cu and Si/SiO_2. Finally, the topside was passivated and 20 μm diameter wells were defined over the TSVs, again with SU-8, but this time in a one-step process.

The fabricated chips therefore had a topside with individually addressable SiNWs in isolated wells connected to the backside through TSVs which were used as the drain and source contacts. The process workflow is depicted in groups in Figure 5.1, Figure 5.2, and Figure 5.3 and detailed in Appendix Table 7.4.

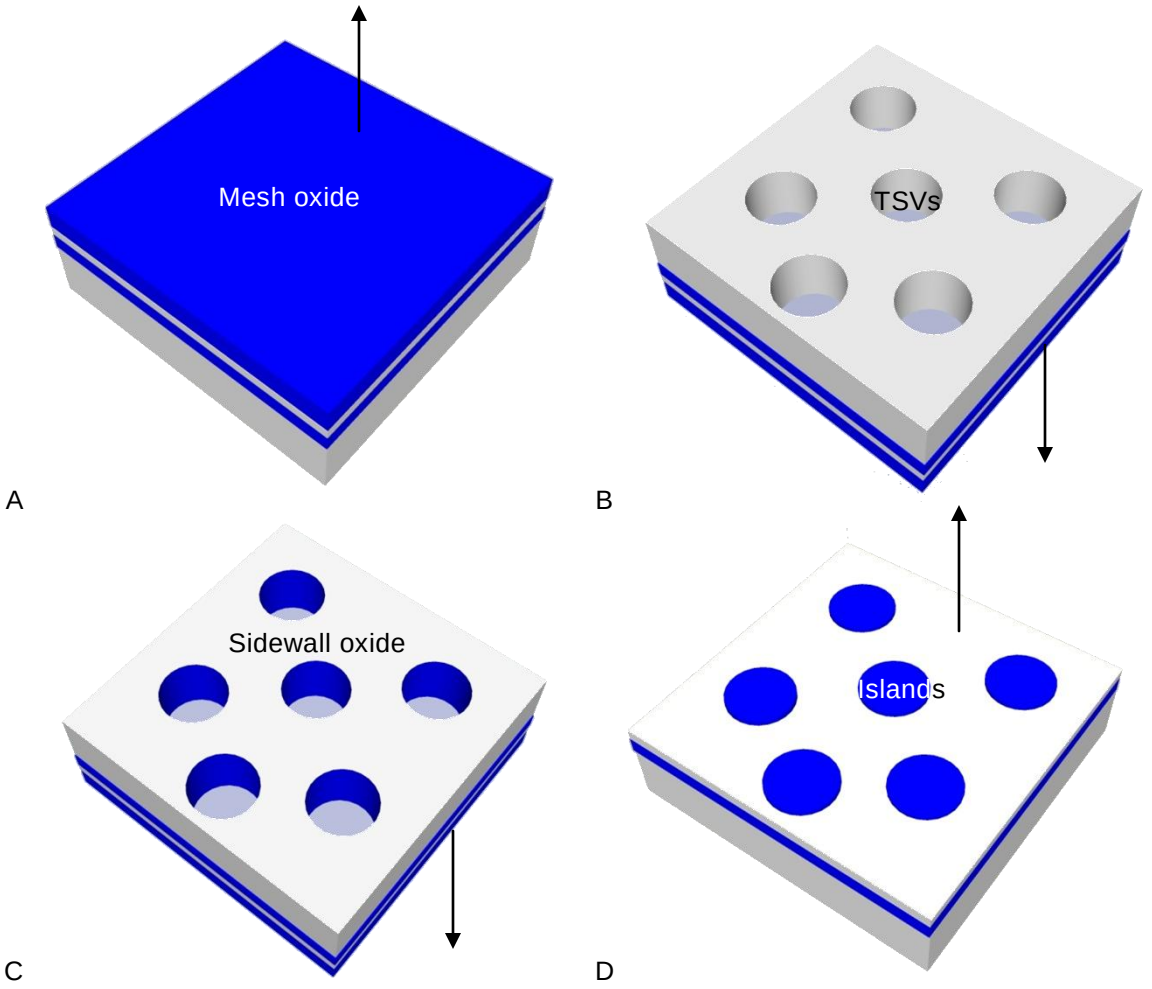

Figure 5.1: Depiction of the high-density array TSV processing workflow

A PECVD oxide was first deposited on the backside (A). Next, the TSVs were etched from the backside up to the PECVD oxide on the topside (B). The sidewalls were then passivated from the backside, again with the PECVD (C). Finally, the PECVD oxide on the topside was removed everywhere except for a region centered on the TSVs (D). The arrow direction indicates the topside.

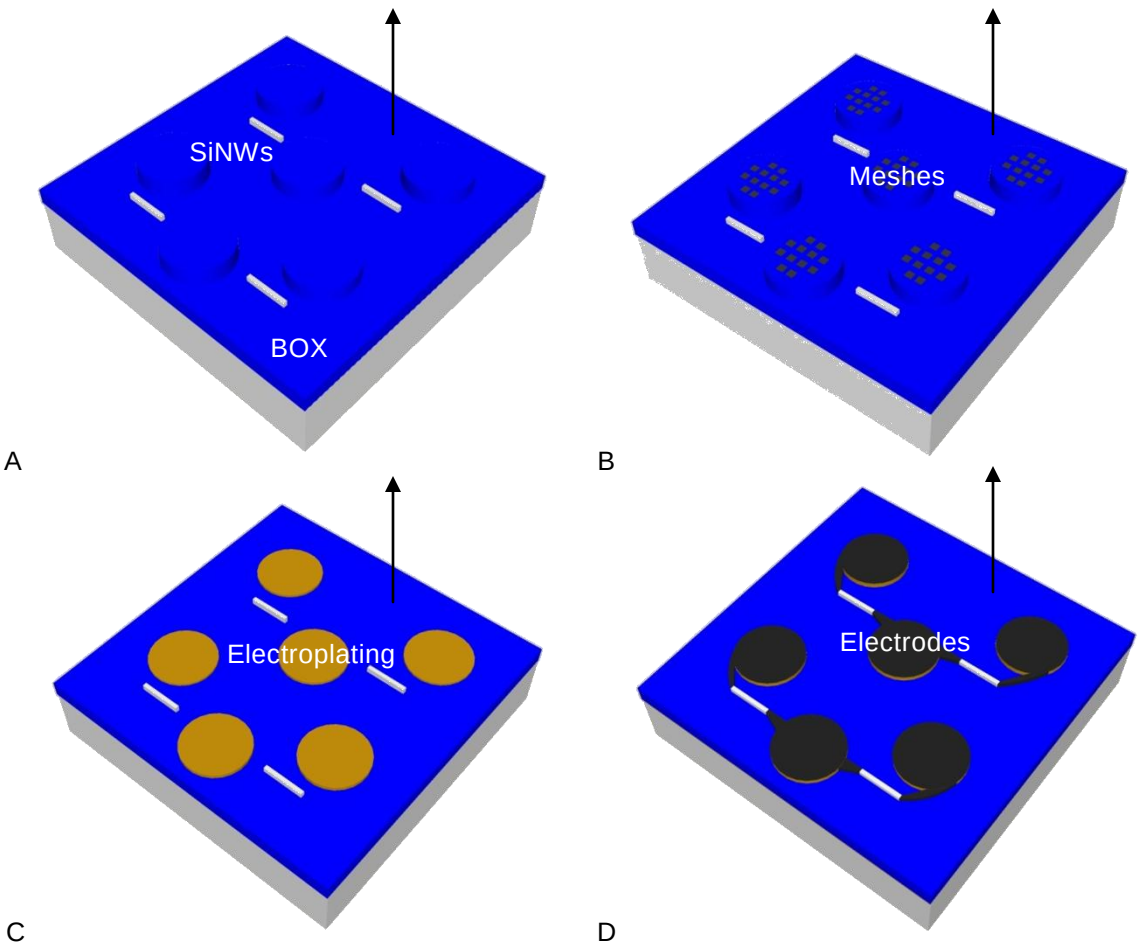

Figure 5.2: Depiction of the high-density array SiNW and metal processing workflow EBL and an ICP were used to pattern and define the SiNWs on the topside (A). Next, the mesh was etched through the PECVD defined oxide from the topside (B). The TSVs were plated, first by using electroplating to pinch off the mesh from the topside and then by using electroplating from the backside (C). Electrodes were then deposited to connect the plated TSVs with the SiNWs (D). The arrow direction indicates the topside.

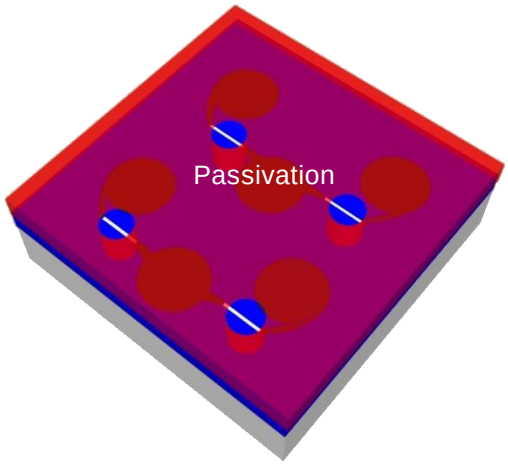

Figure 5.3: Depiction of the completed high-density array with wells

A one-step passivation process defined the wells and protected the electrodes.

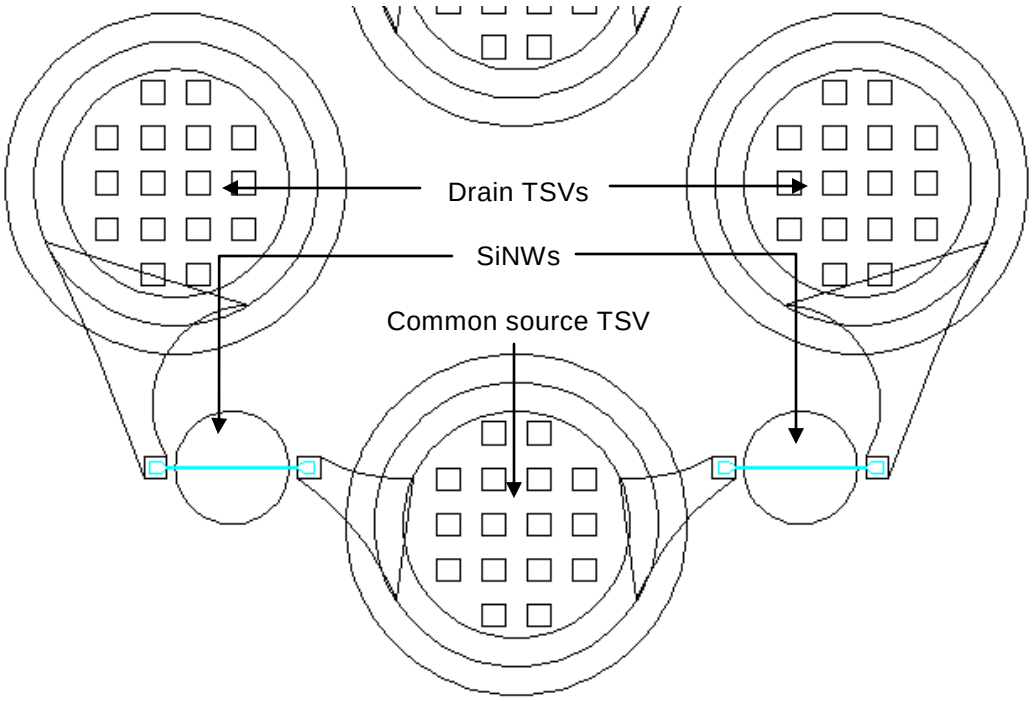

Figure 5.4: CAD layout of a single high-density chip

A close-up of two sensors is shown. The SiNWs have separate drains and share a source.

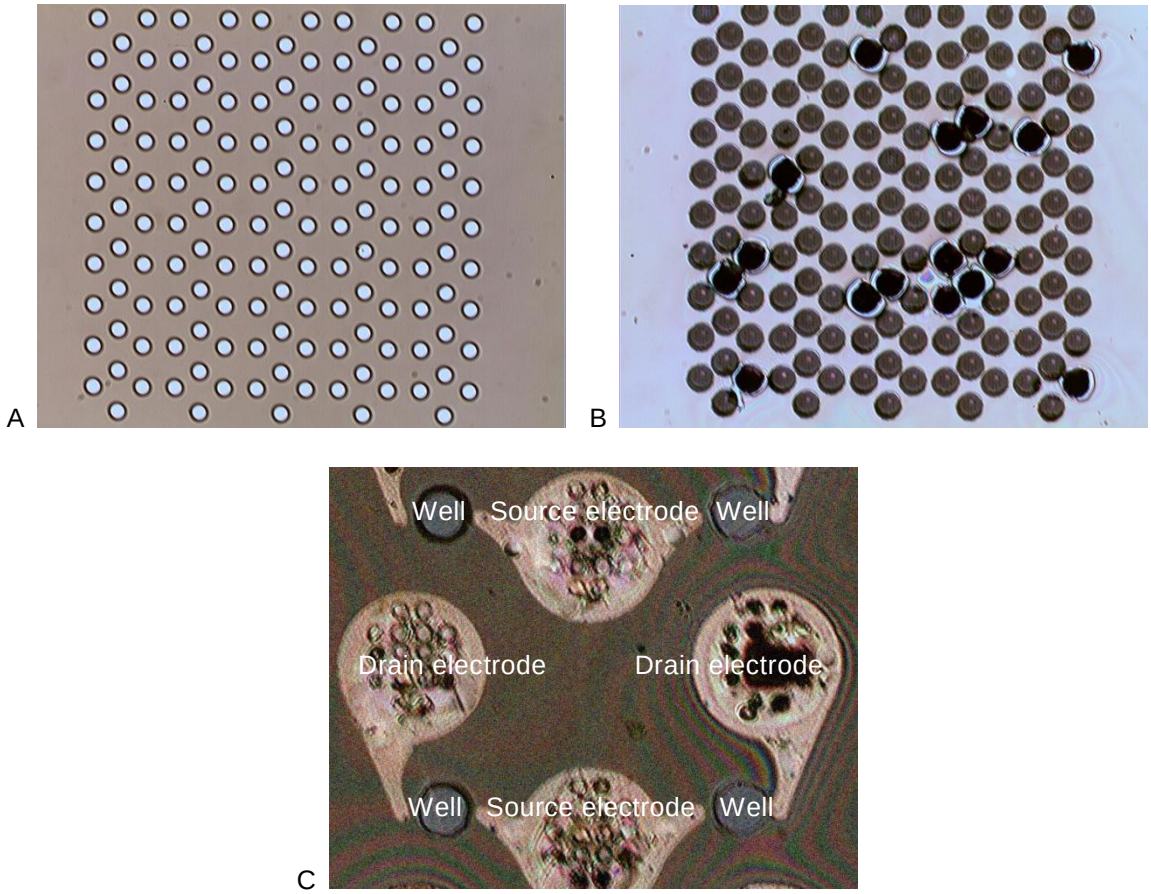

Figure 5.5: Images of a fabricated high-density array chip at various stages

Shown are a 1 x 1 mm of as etched TSVs for a 10 x 10 SiNW array (A), an array of TSVs ready for plating (B), and finally, a group of 4 completed SiNWs with wells (C).

5.3 Characterization Measurements

Again, as for the low-density array, dry and wet measurements were performed. The chip was first electrically characterized in dry conditions and then it was characterized in PBS based wet conditions. There was a unique requirement for probing as the topside with the sensors was no longer the side with the source and drain contacts.

To determine the effects of TSV induced performance degradation, two samples were fabricated in parallel. The first sample (non-plated) was fabricated with all the steps except those required for the TSVs while the second sample (plated) also included all the steps required for the TSVs. The source and drain electrodes of the non-plated sample were probed from the topside Al electrodes while the source and drain TSVs of plated samples were probed from the backside to measure the impact of TSV related processing and the TSVs themselves. The final SU-8 passivation step was excluded in both cases so that both samples would be as similar in fabrication as possible, while still allowing for the non-plated sample to be probed from the topside. This would naturally have not been possible with the SU-8 passivating the topside.

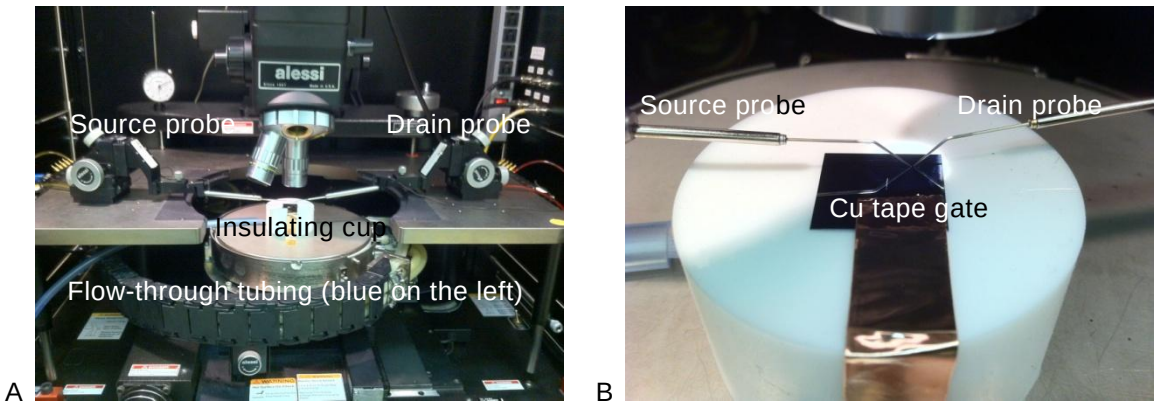

Figure 5.6: Testing setup for high-density array sensing

The test configuration was unique compared to prior configurations because of the need to be able introduce solutions to the topside sensors, but probe the TSVs from the backside. To accomplish this, an insulating cup with a hole in the center held the chip topside facing down while allowing the TSVs to be probed. A cell cloning cylinder

cap with inlet and outlet tubing capped the sample through the hole in the cup. This was essentially an upside down version of the flow-through configuration used in Chapter 4. Cu tape was used to electrically connect the back-gate with the probestation chuck. This configuration was used to measure the plated sample in both dry and wet conditions. The non-plated sample still used the cup and Cu tape, but with the topside facing up to negate any factors associated with the tape.

Standard IV and transconductance curves were measured on both sets of samples. A representative set of curves are shown in Figure 5.7 and Figure 5.8 for the non-plated and plated samples, respectively. V_{DS} = -5 V in the transconductance curves.

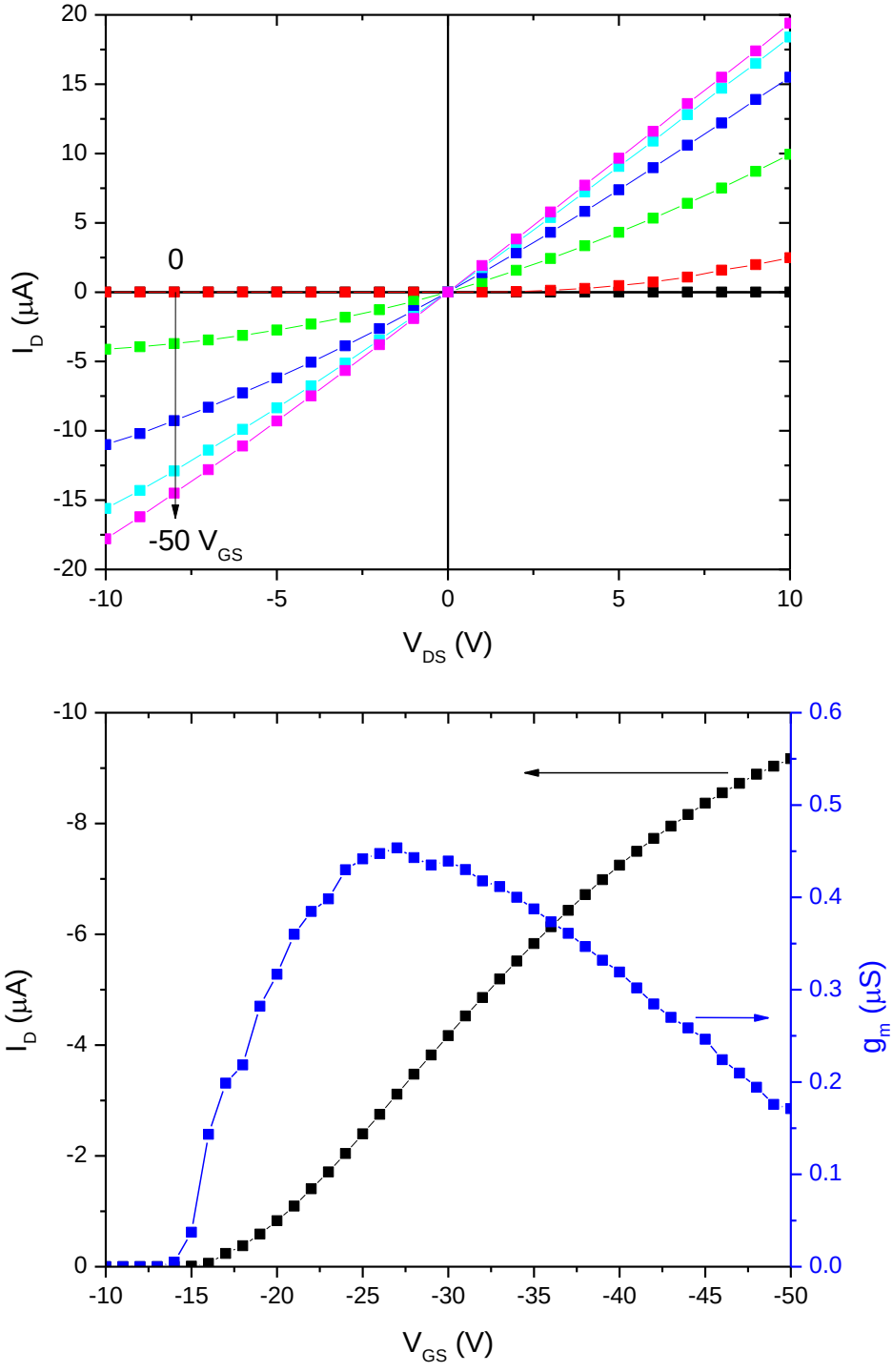

Figure 5.7: Dry IV and I_D and g_m vs. V_{GS} curves for a non-plated high-density array

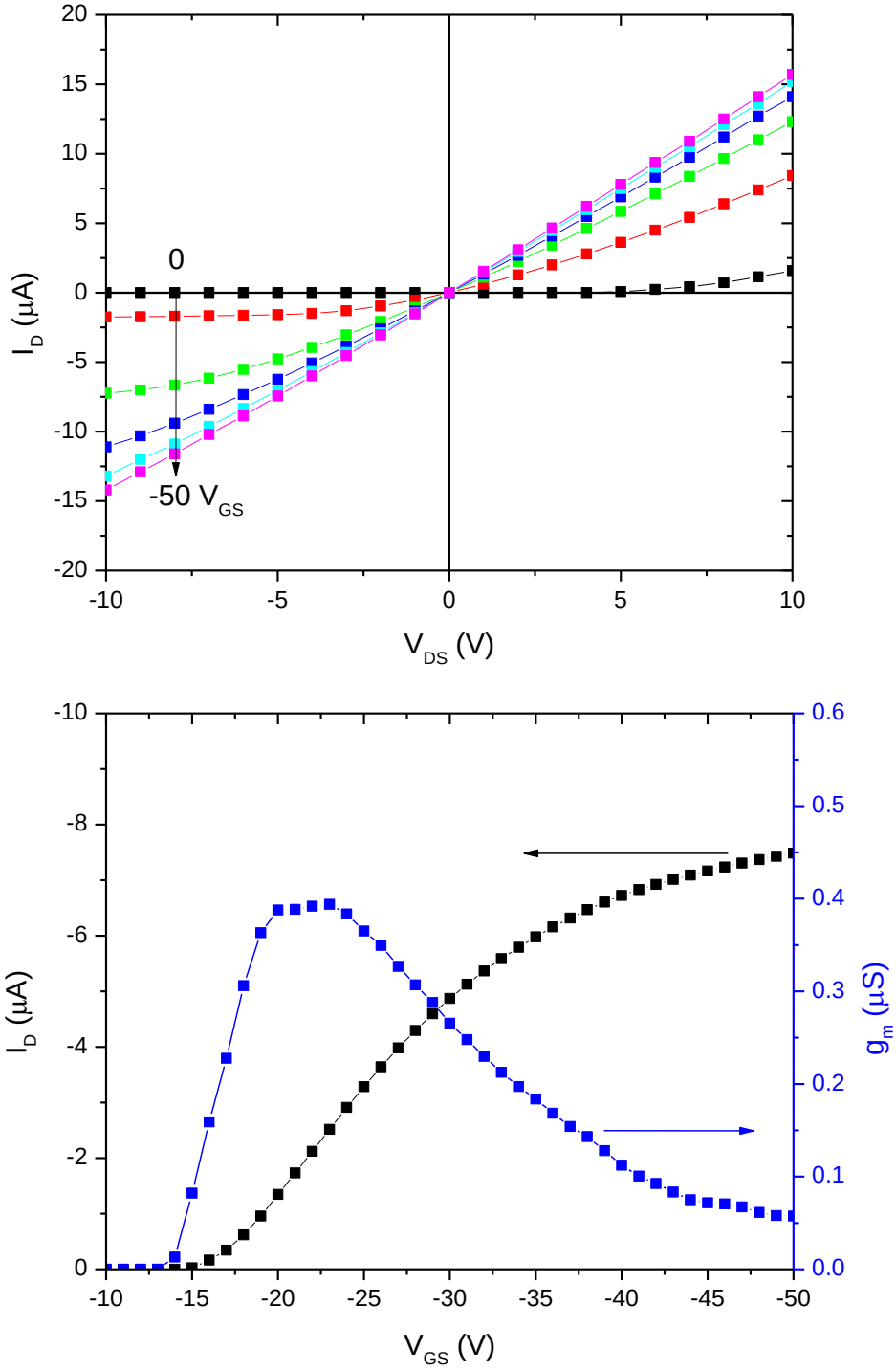

Figure 5.8: Dry IV and I_D and g_m vs. V_{GS} curves for a plated high-density array

There was not a large performance degradation in terms of both I_D and transconductance between the plated and non-plated samples The non-plated sample did generally exhibit higher drive currents (≈10%) and a higher and broader transconductance peak. The drop in I_D is, however, larger than would be expected simply from the added resistance of the drain and source TSVs – which would be about 106 mΩ for two 40 μm diameter x 200 μm Cu cylinders assuming bulk Cu resistivity of $1.68 \cdot 10^{-8}$ Ω·m. The explanation is two-fold. First, the electroplating cannot be expected to produce an electrically perfect Cu TSV, but far more likely, much of the performance degradation arose from the contact resistance between the Cu TSVs and the Al electrodes. It has been previously known that Cu/Al alloys and interfaces may corrode and such an interface may have been formed by the last annealing step. [90] A solution would be to use a single metal for both the TSVs and electrodes. Unfortunately, the plating process with Cu and the Al/Si contact were both well developed in our facility and the performance penalty was accepted.

Nearest-neighbor TSV leakage measurements were also performed. The array design grouped two SiNWs having individual drains with a common source as shown in Figure 5.4. This leakage is defined as the current from a drain TSV to the nearest source TSV to which it is not connected via a SiNW. These leakage currents were more than two of magnitude lower than I_D, suggesting adequate TSV sidewall passivation under typical biases as shown in Figure 5.9.

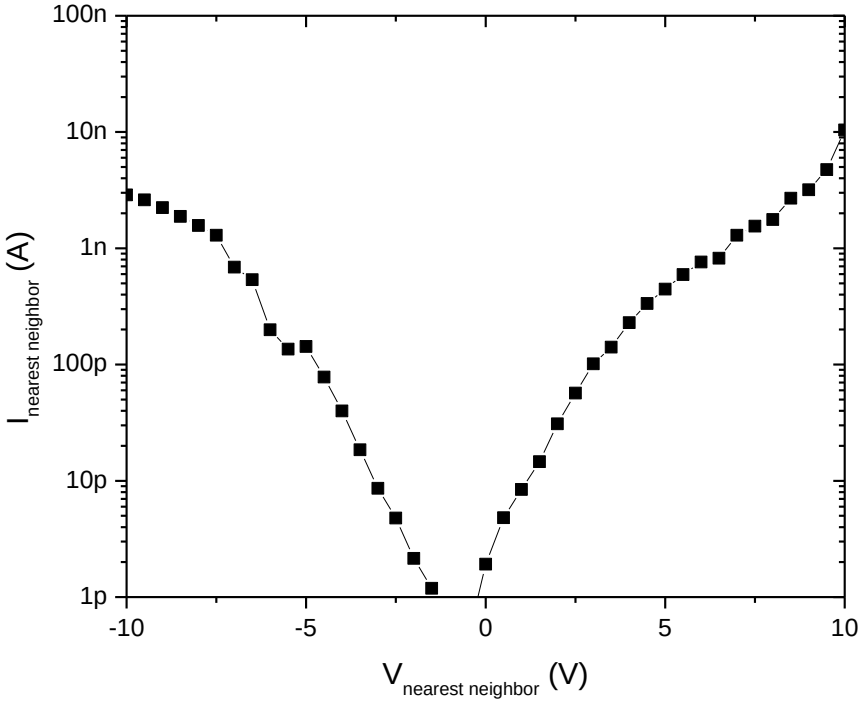

Figure 5.9: Nearest-neighbor TSV leakage

Current values below the sensing limits of the parameter analyzer are cutoff.

5.4 pH Ssensing Measurements

pH sensing measurements in biologically relevant conditions were performed on samples fabricated using the complete process, similar to the test configuration of Chapter 2, but with PBS at five different pH levels rather than three and in a flow-through, rather than a well configuration. The topside of the chip was capped with a 2 mm diameter x 4 mm tall cell cloning cylinder nearly identical to the flow-through setup from Chapter 4 as previously mentioned, but into and out of which six tubes (five inlet and one outlet) were placed. The entire fixture was sealed with mounting adhesive. The

tubing lengths were kept just long enough to extend outside of the probestation enclosure to facilitate rapid exchange of solutions. Each of the five inlet tubes was fitted with a syringe containing 1x PBS at pH levels of 2.8, 5.0, 7.3, 10.9, and 12.3. pH 7.3 PBS was first introduced and a transcondutance measurement was performed at V_{DS} = -5 V to establish an optimal biasing point as in prior tests. [29] Next, pH 2.8 PBS was introduced and a timed measurement run was performed. After an initial settling period, the five PBS solutions with pH values ranging from 2.8 to 12.3 and back down to 2.8 were sequentially introduced approximately every 100 s. The resulting I_D versus time curve is shown in Figure 5.10.

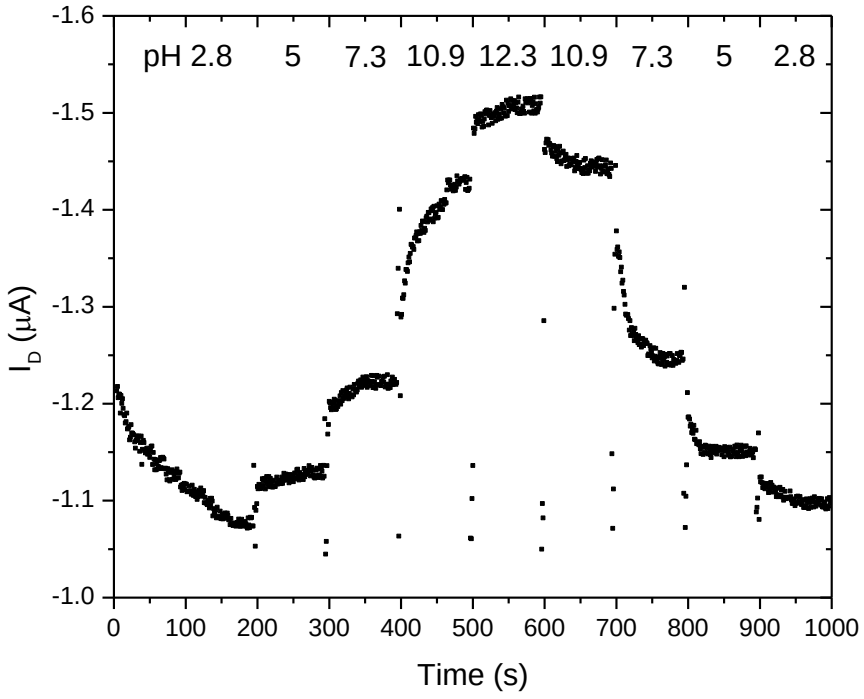

Figure 5.10: Time-dependent response to varying pH solutions

The flow-through configuration again allowed for far lower hysteresis during solution exchanges than the well configuration of Chapter 2. The sensitivity (defined as the change in I_D for a unit change in pH) was ≈50 nA/pH above a pH of 5. The non-linear response of the sensors below a pH of 5 is typical of unfunctionalized SiO_2 surfaces terminating only in hydroxyl groups. [26] The I_D versus pH curve is shown in Figure 5.11.

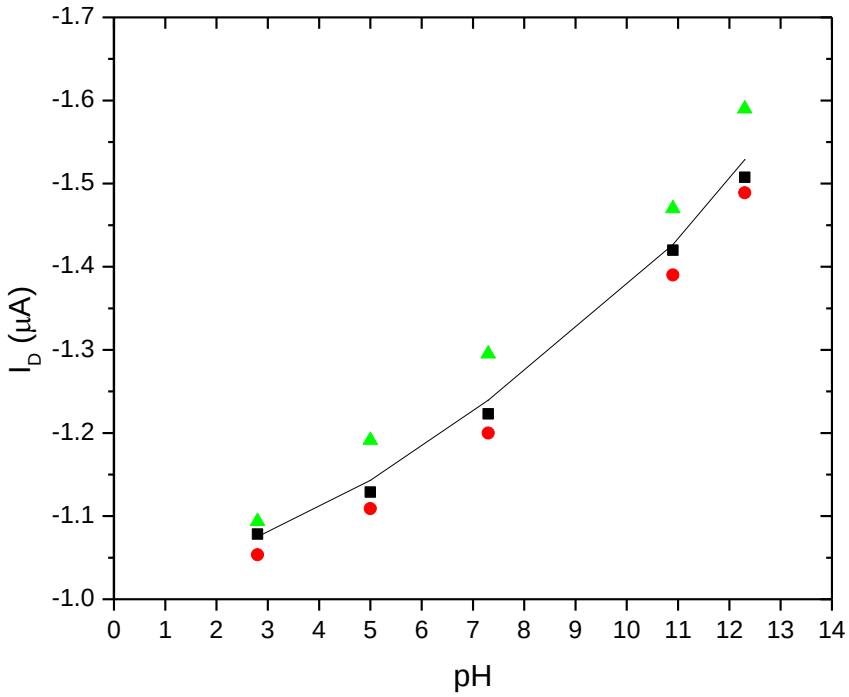

Figure 5.11: I_D versus pH for a high-density array

The square, circle, and triangle are three different devices and the line is the average of the three.

The linear change in I_D with logarithmic changes in H^+ and OH^- concentration is identical to the discussion about log-linear relationships in Chapter 3 and has in fact

been experimentally observed by all SiNW sensors operated in the linear region. [26, 37, 38]

While the high-density array was operated in a flow-through configuration here, it could also be used in a spotting configuration, as in Chapter 3, with the appropriate nano or micro-scale biochemical spotting tool. [91, 92] This was not a readily accessible resource during the course of this work, but there is no inherent limitation toward using the tool. In fact, this would be the most logical configuration of an electronic microplate with numerous individually addressable sensors as it would bypass the aforementioned complexities of microfluidics.

5.5 Refinements

There remains room to maximize yield, which was roughly 10 % compared to the better than 90 % yield with the low-density array. The drop relative to the test and low-density arrays was the result of the substantial increase in fabrication complexity. The two most common causes of sensor failure were either a poorly defined mesh that led to failed electroplating of that TSV or, more commonly, a short from the source or drain to the gate. The cause of the source or drain to gate shorts was the electroplated copper coming into contact with the carrier layer Si near the topside during pinch-off due to poor alignment of the island or mesh, leading to removal of the relatively thin BOX layer during either the BOE etching of the islands or RIE etching of the mesh, respectively or damage to the passivating sidewall oxide. A schematic comparison of the plated and non-plated samples is available in Figure 7.1 of the Appendix.

These are not fundamental limitations of the process conceptually, but rather the result of the alignment limits of the available optical lithography tools over the multiple lithography steps under fairly tight tolerances for the high-density array (≈5 μm for all patterning steps in sum). This was made more challenging over previous work because of the addition of the islands, the use of SOI wafers, and the need to have working sensors at the end. A lithography setup with better alignment and resolution capabilities along with, and equally importantly, better controlled etch process flows would mitigate or eliminate these issues, even in a multi-user facility.

Recent industry developments in non-planar CMOS and 3DS technologies suggest that such a configuration would be entirely reasonable to manufacture in a large-scale and commercially viable process with perhaps even a near complete mitigation of the any performance tradeoffs. [93, 94]

5.6 Summary

This chapter discussed the fabrication and characterization of a high-density SiNW sensor array using a CMOS compatible process incorporating TSVs. Fundamental electrical measurements demonstrated that the sensor array could function as a pH sensor in PBS.

6 CONCLUSIONS AND FUTURE WORK

6.1 Summary

The work described in this dissertation really started with the broad goal of visualizing what a next-generation biosensing platform might look like. The end result, the idea of the electronic microplate, is a combination of the tremendous advances in biology and microelectronics over the last half-century.

The key contributions of this work were:

- Envisioning an idea for a highly scalable general purpose next-generation biosensing platform
- Establishing a fully top-down CMOS compatible workflow for label-free sensor array fabrication using methods used in emerging non-planar devices
- Demonstrating the first label-free delineation of healthy and cancerous ovarian epithelial cell lines using intracellular contents
- Demonstrating the first label-free capture and detection of functionalized SPIONs
- Establishing the workflow for and demonstrating the first truly high-density label-free sensor array

6.2 Future Work

Perhaps the most exciting aspect of starting on a new idea are the possibilities that lie in extending that idea. While the work described in this dissertation implemented fundamental elements of the electronic microplate, there are numerous contributions that remain to be made, as would be expected of most courses of work. These extensions can be categorized into two parallel groups. The first is in applications and the second is in scaling the sensing and electronics layers.

In terms of applications, there are many current bioassays which might be directly transferable to a label-free technology. Examples range from gene sequencing to current clinical assays such as lipid profile tests. Even entire processes such as polymerase chain reactions could be carried out on the electronic microplate. There is really no fundamental limit to what bioassays could be transferred to this electronic sensing platform.

In terms of scaling the components of the platform, fleshing out the constituent layers will certainly be worthwhile. First would be the development of reliable and high-density compliant interconnects suited for this role. Second would be the development of a general purpose electronics layer that can control a variety of electronic microplates possessing a broad range of sensing capabilities.

One general suggestion would be to outsource key technologies after demonstration on the fabrication side while keeping biological development in-house. There is a very large delta in the capabilities of multi-user cleanrooms and foundries. It would be ideal to initially use the flexibility afforded by multi-user cleanrooms before transferring the designs to the robust fabrication afforded by foundries.

Physically, the sensing layer and the electronics layer are rather simple elements that are enablers for a multitude of sensing applications. It might perhaps even be wise to make transferring the fabrication of the sensing layer to a foundry the first priority and the electronics layer the second priority. With a reliable source of the physical components, there would be opportunities to fully explore the real capabilities of this platform – which really lie in exciting new biochemical sensing applications. There is no doubt tremendous potential in applications such as ubiquitous clinical screenings, biological research, point-of-care testing, food safety, as well as countless other areas.

7 APPENDIX

7.1 Device Si, BOX, and HSQ Etch Rates

Table 7.1: Device Si, BOX, and HSQ etch rates

Spin-Chip	Average Etched Materials by SOE (nm)			Etch Rate (nm/s)		
	Si	BOX	HSQ	Si	BOX	HSQ
1-1	70.5	1.6	21.1	5.9	0.8	1.5
1-2	70.5	5.3	27.8	5.9	1.1	1.6
1-3	70.5	7.9	34.9	5.9	1.0	1.7
Control	0.0	0.0	0.0	0.0	0.0	0.0
2-5	70.5	1.6	17.6	5.9	0.8	1.3
2-6	70.5	6.6	30.1	5.9	1.3	1.8
2-7	70.5	8.0	30.0	5.9	1.0	1.5
Control	0.0	0.0	0.0	0.0	0.0	0.0

Spin-Chip	Average Etched Materials by BOE (nm)			Etch Rate (nm/s)		
	Si	BOX	HSQ	Si	BOX	HSQ
1-1	0.0	7.9	21.4	0.0	2.0	5.3
1-2	0.0	4.7	14.2	0.0	2.4	7.1
1-3	0.0	4.0	9.5	0.0	2.0	4.7
Control	0.0	0.0	0.0	0.0	0.0	0.0
2-5	0.0	7.3	18.3	0.0	1.8	4.6
2-6	0.0	5.4	9.4	0.0	2.7	4.7
2-7	0.0	5.1	4.6	0.0	2.5	2.3
Control	0.0	0.0	0.0	0.0	0.0	0.0

Spin	Average Etch Rates (nm/s), RAMA_SI			Standard Deviation (nm/s)		
	Si	BOX	HSQ	Si	BOX	HSQ
1	5.9	0.9	1.6	0.0	0.1	0.1
2	5.9	1.0	1.5	0.0	0.3	0.3
Cumulative	5.9	1.0	1.6	0.0	0.2	0.2

Table 7.1 details the characterization of Si, BOX, and HSQ etch rates during dry etching in the ICP and wet etching in BOE.

7.2 Process Development Fabrication Workflow

Table 7.2: Process development fabrication workflow

Step	Chemical/Tool	Process
SiNW	6% HSQ	5000rpm, 2500rpm/s, 40s
		250C, 60s
		RD6, 60s, 10% RD6, 60s
	EBL	SNR082208
	STS SOE	RAMA_SI, 18s
RTP Oxide	AET RTP	RAMA_O, O2, 900C, 2min, ramp up in 1min
Metallization		5s BOE
	NR9-1500PY	150C hotplate, 60s
		589mJ, 365nm
		100C hotplate, 60s
		RD6, 12s
	E-beam	Al, 100nm, 2A/s
RTP Annealing	AET RTP	RAMA_M, FG, 400C, 5min, ramp up in 1 min
Passivation	SU-8 2002	2000rpm, 300rpm/s, 30s
		95C hotplate, 90s
		90mJ, 365nm
		95C hotplate, 60s
		SU-8 developer, 60s

Table 7.2 details the workflow used to fabricate the devices described in Chapter 2. All the tools were part of the Georgia Institute of Technology Nanotechnology Research Center.

7.3 Low-Density Array Fabrication Workflow

Table 7.3: Low-density array fabrication workflow

Step	Chemical/Tool	Process
SiNW	2% HSQ	4000rpm, 2000rpm/s, 40s
		180C, 3min
		RD6, 60s, 10% RD6, 60s
	EBL	SNR031009
	STS SOE	RAMA_SI, 18s
RTP Oxide	AET RTP	RAMA_O, O2, 900C, 2min, ramp up in 1min
Metallization		5s BOE
	NR9-1500PY	150C hotplate, 60s
		589mJ, 365nm
		100C hotplate, 60s
		RD6, 12s
	E-beam	Al, 100nm, 2A/s
RTP Annealing	AET RTP	RAMA_M, FG, 450C, 5min, ramp up in 1 min
Passivation	SU-8 2002	2000rpm, 300rpm/s, 30s
		95C hotplate, 90s
		90mJ, 365nm
		95C hotplate, 60s
		SU-8 developer, 60s
Wells	SU-8 2050	1700rpm, 300rpm/s, 30s
		65C oven, 5min, 95C oven, 15min
		230mJ, 365nm
		65C oven, 3min, 95C oven, 9min
		SU-8 developer, 8min

Table 7.3 details the workflow used to fabricate the devices described in Chapters 3 and 4. All the tools were part of the Georgia Institute of Technology Nanotechnology Research Center.

7.4 High-Density Array Fabrication Workflow

Table 7.4: High-density array fabrication workflow

Step	Chemical/Tool	Process
Mesh Oxide	Unaxis PEVCD	RAMA_OX, 33min
TSV	NR5-8000	600rpm, 100rpm/s, 50s
		100C oven, 15min
		554mJ, 365nm
		75C oven, 8min
		RD6, 50s
	STS ICP	RAMA_TSV, ~700 cycles
SiO2 Island	SC1827	2500rpm, 500rpm/s, 30s
		100C hotplate, 3min
		185mJ, 365nm
		RD6, 40s
	BOE	~6min
Sidewall Passivation	Unaxis PECVD	RAMA_OX, 33min
SiNW	2% HSQ	4000rpm, 2000rpm/s, 40s
		180C, 3min
	EBL	SNR012210
		RD6, 60s, 10% RD6, 60s
	STS SOE	RAMA_SI, 18s
RTP Oxide	AET RTP	RAMA_O, O2, 900C, 2min, ramp up in 1min
Mesh	NR9-1500PY	800rpm, 500rpm/s, 40s
		150C hotplate, 60s
		589mJ, 365nm
		100C hotplate, 60s
		RD6, 24s
	Vision Oxide 1	STDOX_200, ~60min
Seed Layer	NR9-1500PY	5000rpm, 1000rpm/s, 40s
		150C hotplate, 60s
		589mJ, 365nm
		100C hotplate, 60s
		RD6, 12s
	E-beam	Cr/Au, 10/1000nm, 2A/s
Electroplating	Cu Plating	3mA 0-10min, 6mA 10min-8hr
Metallization		5s BOE
	NR9-1500PY	5000rpm, 1000rpm/s, 40s
		150C hotplate, 60s
		589mJ, 365nm
		100C hotplate, 60s
		RD6, 12s
	E-beam	Al, 100nm, 2A/s
RTP Annealing	AET RTP	RAMA_M, FG, 400C, 5min, ramp up in 1 min
Passivation	SU-8 2002	2000rpm, 300rpm/s, 30s
		95C hotplate, 90s
		90mJ, 365nm
		95C hotplate, 60s
		SU-8 developer, 60s

Table 7.4 details the workflow used to fabricate the devices described in Chapter 5. All the tools were part of the Georgia Institute of Technology Nanotechnology Research Center.

7.5 Plated and Non-Plated High-Density Arrays

Non-plated side-view:

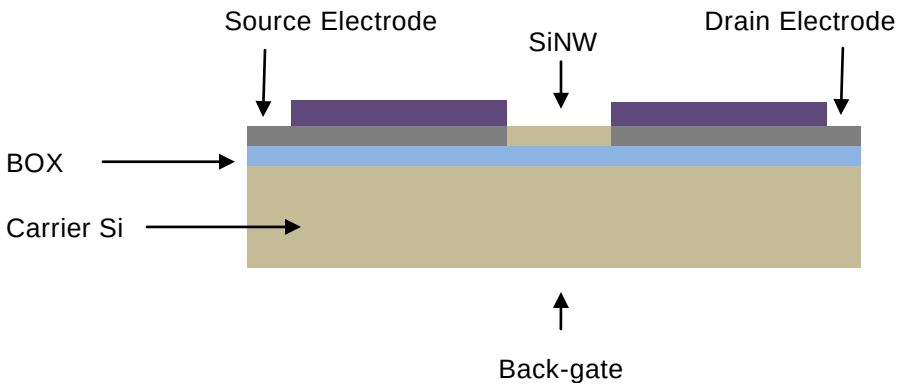

Plated side-view with normal and damaged TSVs:

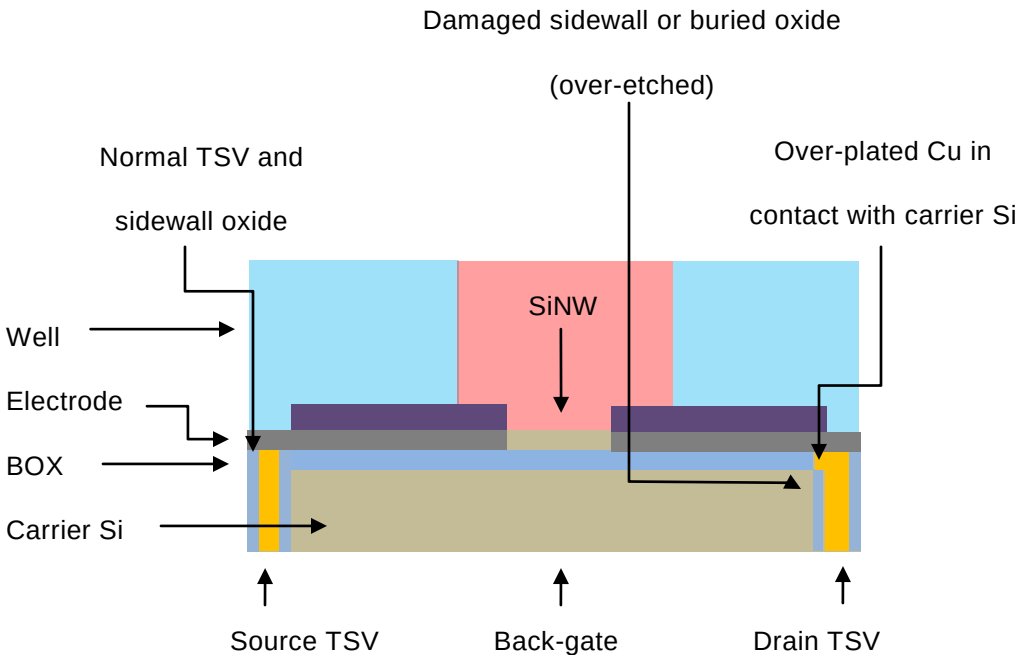

Figure 7.1: Plated and non-plated high-density arrays

8 REFERENCES

[1] J. M. Niloff, *et al.*, "Ca125-Antigen Levels in Obstetric and Gynecologic Patients," *Obstetrics and Gynecology,* vol. 64, pp. 703-707, 1984.

[2] P. A. Canney, *et al.*, "Ovarian-Cancer Antigen Ca125 - a Prospective Clinical-Assessment of Its Role as a Tumor-Marker," *British Journal of Cancer,* vol. 50, pp. 765-769, 1984.

[3] W. J. Catalona, *et al.*, "Comparison of Digital Rectal Examination and Serum Prostate-Specific Antigen in the Early Detection of Prostate-Cancer - Results of a Multicenter Clinical-Trial of 6,630 Men," *Journal of Urology,* vol. 151, pp. 1283-1290, May 1994.

[4] W. J. Catalona, *et al.*, "Prostate cancer detection in men with serum PSA concentrations of 2.6 to 4.0 ng/mL and benign prostate examination - Enhancement of specificity with free PSA measurements," *Journal of the American Medical Association,* vol. 277, pp. 1452-1455, May 14 1997.

[5] A. B. Lowenfels, *et al.*, "Pancreatitis and the Risk of Pancreatic-Cancer," *New England Journal of Medicine,* vol. 328, pp. 1433-1437, May 20 1993.

[6] R. T. P. Poon, *et al.*, "Clinical implications of circulating angiogenic factors in cancer patients," *Journal of Clinical Oncology,* vol. 19, pp. 1207-1225, Feb 15 2001.

[7] Z. Zhang, *et al.*, "Three biomarkers identified from serum proteomic analysis for the detection of early stage ovarian cancer," *Cancer Research,* vol. 64, pp. 5882-5890, Aug 15 2004.

[8] R. A. Smith, *et al.*, "American Cancer Society guidelines for the early detection of cancer, 2004," *Cancer Journal for Clinicians,* vol. 54, pp. 41-52, Jan-Feb 2004.

[9] T. J. Hudson, *et al.*, "International network of cancer genome projects," *Nature,* vol. 464, pp. 993-998, Apr 15 2010.

[10] G. R. Bignell, *et al.*, "Signatures of mutation and selection in the cancer genome," *Nature,* vol. 463, pp. 893-U61, Feb 18 2010.

[11] M. R. Stratton, *et al.*, "The cancer genome," *Nature,* vol. 458, pp. 719-724, Apr 9 2009.

[12] P. J. Mintz, *et al.*, "Fingerprinting the circulating repertoire of antibodies from cancer patients," *Nature Biotechnology,* vol. 21, pp. 57-63, Jan 2003.

[13] J. K. Pai, *et al.*, "Inflammatory markers and the risk of coronary heart disease in men and women.," *New England Journal of Medicine,* vol. 351, pp. 2599-2610, Dec 16 2004.

[14] A. D. Weston and L. Hood, "Systems biology, proteomics, and the future of health care: Toward predictive, preventative, and personalized medicine," *Journal of Proteome Research,* vol. 3, pp. 179-196, Mar-Apr 2004.

[15] E. Engvall and P. Perlmann, "Enzyme-Linked Immunosorbent Assay, Elisa .3. Quantitation of Specific Antibodies by Enzyme-Labeled Anti-Immunoglobulin in Antigen-Coated Tubes," *Journal of Immunology,* vol. 109, pp. 129-&, 1972.

[16] R. J. Lipshutz, *et al.*, "High density synthetic oligonucleotide arrays," *Nature Genetics,* vol. 21, pp. 20-4, Jan 1999.

[17] X. H. Gao, *et al.*, "In vivo cancer targeting and imaging with semiconductor quantum dots," *Nature Biotechnology,* vol. 22, pp. 969-976, Aug 2004.

[18] N. L. Rosi and C. A. Mirkin, "Nanostructures in biodiagnostics," *Chemical Reviews,* vol. 105, pp. 1547-1562, Apr 2005.

[19] W. H. Robinson, *et al.*, "Autoantigen microarrays for multiplex characterization of autoantibody responses," *Nature Medicine,* vol. 8, pp. 295-301, Mar 2002.

[20] P. L. Felgner, *et al.*, "A Burkholderia pseudomallei protein microarray reveals serodiagnostic and cross-reactive antigens," *Proceedings of the National Academy of Sciences of the United States of America,* vol. 106, pp. 13499-13504, Aug 11 2009.

[21] Y. Xing, *et al.*, "Bioconjugated quantum dots for multiplexed and quantitative immunohistochemistry," *Nature Protocols,* vol. 2, pp. 1152-1165, 2007.

[22] M. Y. Han, *et al.*, "Quantum-dot-tagged microbeads for multiplexed optical coding of biomolecules," *Nature Biotechnology,* vol. 19, pp. 631-635, Jul 2001.

[23] X. M. Qian, *et al.*, "In vivo tumor targeting and spectroscopic detection with surface-enhanced Raman nanoparticle tags," *Nature Biotechnology,* vol. 26, pp. 83-90, Jan 2008.

[24] S. X. Leng, *et al.*, "ELISA and multiplex technologies for cytokine measurement in inflammation and aging research," *Journals of Gerontology Series a-Biological Sciences and Medical Sciences,* vol. 63, pp. 879-884, Aug 2008.

[25] J. Fritz, *et al.*, "Electronic detection of DNA by its intrinsic molecular charge," *Proceedings of the National Academy of Sciences of the United States of America,* vol. 99, pp. 14142-14146, Oct 29 2002.

[26] Y. Cui, *et al.*, "Nanowire nanosensors for highly sensitive and selective detection of biological and chemical species," *Science,* vol. 293, pp. 1289-1292, Aug 17 2001.

[27] Z. Li, *et al.*, "Sequence-specific label-free DNA sensors based on silicon nanowires," *Nano Letters,* vol. 4, pp. 245-247, Feb 2004.

[28] A. Janshoff, *et al.*, "Piezoelectric mass-sensing devices as biosensors - An alternative to optical biosensors?," *Angewandte Chemie-International Edition,* vol. 39, pp. 4004-4032, 2000.

[29] E. Stern, *et al.*, "Label-free immunodetection with CMOS-compatible semiconducting nanowires," *Nature,* vol. 445, pp. 519-522, Feb 1 2007.

[30] C. D. Corso, *et al.*, "Real-time detection of mesothelin in pancreatic cancer cell line supernatant using an acoustic wave immunosensor," *Cancer Detection and Prevention,* vol. 30, pp. 180-187, 2006.

[31] T. Braun, *et al.*, "Quantitative time-resolved measurement of membrane protein-ligand interactions using microcantilever array sensors," *Nature Nanotechnology,* vol. 4, pp. 179-185, Mar 2009.

[32] M. A. Cooper and V. T. Singleton, "A survey of the 2001 to 2005 quartz crystal microbalance biosensor literature: applications of acoustic physics to the analysis of biomolecular interactions," *Journal of Molecular Recognition,* vol. 20, pp. 154-184, May-Jun 2007.

[33] F. Vollmer, *et al.*, "Single virus detection from the reactive shift of a whispering-gallery mode," *Proceedings of the National Academy of Sciences of the United States of America,* vol. 105, pp. 20701-20704, Dec 30 2008.

[34] Y. L. Bunimovich, *et al.*, "Quantitative real-time measurements of DNA hybridization with alkylated nonoxidized silicon nanowires in electrolyte solution," *Journal of the American Chemical Society,* vol. 128, pp. 16323-16331, Dec 20 2006.

[35] B. S. Doyle, *et al.*, "High performance fully-depleted tri-gate CMOS transistors," *IEEE Electron Device Letters,* vol. 24, pp. 263-265, Apr 2003.

[36] C. H. Lin, *et al.*, "Non-Planar Device Architecture for 15nm Node: FinFET or Trigate?," *2010 IEEE International Soi Conference,* 2010.

[37] P. R. Nair and M. A. Alam, "Design considerations of silicon nanowire biosensors," *IEEE Transactions on Electron Devices,* vol. 54, pp. 3400-3408, Dec 2007.

[38] P. R. Nair and M. A. Alam, "Screening-limited response of nanobiosensors," *Nano Letters,* vol. 8, pp. 1281-1285, May 2008.

[39] E. Stern, *et al.*, "Importance of the debye screening length on nanowire field effect transistor sensors," *Nano Letters,* vol. 7, pp. 3405-3409, Nov 2007.

[40] P. Bergveld, "Development of an Ion-Sensitive Solid-State Device for Neurophysiological Measurements," *IEEE Transactions on Biomedical Engineering,* vol. Bm17, pp. 70-&, 1970.

[41] J. Go, *et al.*, "Beating the Nernst limit of 59mV/pH with Double-Gated Nano-Scale Field-Effect Transistors and Its Applications to Ultra-Sensitive DNA Biosensors," *2010 International Electron Devices Meeting - Technical Digest,* 2010.

[42] M. N. Bobrow, *et al.*, "Catalyzed Reporter Deposition, a Novel Method of Signal Amplification - Application to Immunoassays," *Journal of Immunological Methods,* vol. 125, pp. 279-285, Dec 20 1989.

[43] M. A. Unger, *et al.*, "Monolithic microfabricated valves and pumps by multilayer soft lithography," *Science,* vol. 288, pp. 113-116, Apr 7 2000.

[44] T. Thorsen, *et al.*, "Microfluidic large-scale integration," *Science,* vol. 298, pp. 580-584, Oct 18 2002.

[45] J. F. Zhong, *et al.*, "A microfluidic processor for gene expression profiling of single human embryonic stem cells," *Lab on a Chip,* vol. 8, pp. 68-74, 2008.

[46] T. M. Squires and S. R. Quake, "Microfluidics: Fluid physics at the nanoliter scale," *Reviews of Modern Physics,* vol. 77, pp. 977-1026, Jul 2005.

[47] P. E. Sheehan and L. J. Whitman, "Detection limits for nanoscale biosensors," *Nano Letters,* vol. 5, pp. 803-807, Apr 2005.

[48] G. F. Zheng, *et al.*, "Multiplexed electrical detection of cancer markers with nanowire sensor arrays," *Nature Biotechnology,* vol. 23, pp. 1294-1301, Oct 2005.

[49] J. H. Lai, *et al.*, "A 'mesh' seed layer for improved through-silicon-via fabrication," *Journal of Micromechanics and Microengineering,* vol. 20, pp. -, Feb 2010.

[50] M. S. Bakir, *et al.*, "Sea of leads (SoL) ultrahigh density wafer-level chip input/output interconnections for gigascale integration (GSI)," *IEEE Transactions on Electron Devices*, vol. 50, pp. 2039-2048, Oct 2003.

[51] L. Hood, *et al.*, "Systems biology and new technologies enable predictive and preventative medicine," *Science*, vol. 306, pp. 640-643, Oct 22 2004.

[52] H. Kitano, "Systems biology: A brief overview," *Science*, vol. 295, pp. 1662-1664, Mar 1 2002.

[53] G. N. Ling, *et al.*, "Low Paramagnetic-Ion Content in Cancer-Cells - Its Significance in Cancer-Detection by Magnetic-Resonance-Imaging," *Physiological Chemistry and Physics and Medical Nmr*, vol. 22, pp. 1-14, 1990.

[54] K. E. Scarberry, *et al.*, "Magnetic nanoparticle-peptide conjugates for in vitro and in vivo targeting and extraction of cancer cells," *Journal of the American Chemical Society*, vol. 130, pp. 10258-10262, Aug 6 2008.

[55] J. U. Knickerbocker, *et al.*, "3-D silicon integration and silicon packaging technology using silicon through-vias," *IEEE Journal of Solid-State Circuits*, vol. 41, pp. 1718-1725, Aug 2006.

[56] O. Tabata, *et al.*, "Anisotropic Etching of Silicon in Tmah Solutions," *Sensors and Actuators a-Physical*, vol. 34, pp. 51-57, Jul 1992.

[57] W. Z. Xiong, *et al.*, "Improvement of FinFET electrical characteristics by hydrogen annealing," *IEEE Electron Device Letters*, vol. 25, pp. 541-543, Aug 2004.

[58] A. E. Grigorescu and C. W. Hagen, "Resists for sub-20-nm electron beam lithography with a focus on HSQ: state of the art," *Nanotechnology*, vol. 20, Jul 22 2009.

[59] Y. Wu, *et al.*, "Single-crystal metallic nanowires and metal/semiconductor nanowire heterostructures (vol 430, pg 61, 2004)," *Nature*, vol. 430, pp. 704-704, Aug 5 2004.

[60] D. W. Wang, *et al.*, "Silicon p-FETs from ultrahigh density nanowire arrays," *Nano Letters*, vol. 6, pp. 1096-1100, Jun 2006.

[61] Y. Cheng, *et al.*, "Mechanism and Optimization of pH Sensing Using SnO(2) Nanobelt Field Effect Transistors," *Nano Letters*, vol. 8, pp. 4179-4184, Dec 2008.

[62] X. P. A. Gao, *et al.*, "Subthreshold Regime has the Optimal Sensitivity for Nanowire FET Biosensors," *Nano Letters*, vol. 10, pp. 547-552, Feb 2010.

[63] R. F. Pierret, *Semiconductor fundamentals*. Reading, Mass.: Addison-Wesley, 1983.

[64] I. Heller, *et al.*, "Optimizing the Signal-to-Noise Ratio for Biosensing with Carbon Nanotube Transistors," *Nano Letters,* vol. 9, pp. 377-382, Jan 2009.

[65] E. Stern and Yale University. (2007). *Label-free sensing with semiconducting nanowires*. Available: http://gateway.proquest.com/openurl?url_ver=Z39.88-2004&rft_val_fmt=info:ofi/fmt:kev:mtx:dissertation&res_dat=xri:pqdiss&rft_dat=xri:pqdiss:3267367

[66] F. L. Yang, *et al.*, "5nm-gate nanowire FinFET," *2004 Symposium on VLSI Technology, Digest of Technical Papers,* pp. 196-197, 2004.

[67] M. M. H. Iqbal, *et al.*, "The Nanoscale Silicon Accumulation-Mode MOSFET-A Comprehensive Numerical Study," *IEEE Transactions on Electron Devices,* vol. 55, pp. 2946-2959, Nov 2008.

[68] R. F. Pierret, *Semiconductor fundamentals*, 2nd ed. Reading, Mass.: Addison-Wesley Pub. Co., 1988.

[69] Y. K. Choi, *et al.*, "FinFET process refinements for improved mobility and gate work function engineering," *International Electron Devices 2002 Meeting, Technical Digest,* pp. 259-262, 2002.

[70] J. S. Lee, *et al.*, "Hydrogen annealing effect on DC and low-frequency noise characteristics in CMOS FinFETs," *IEEE Electron Device Letters,* vol. 24, pp. 186-188, Mar 2003.

[71] R. Ravindran, *et al.*, "Permittivity enhancement of aluminum oxide thin films with the addition of silver nanoparticles," *Applied Physics Letters,* vol. 89, Dec 25 2006.

[72] P. Bergveld, "The Development and Application of Fet-Based Biosensors," *Biosensors,* vol. 2, pp. 15-33, 1986.

[73] J. D. Wulfkuhle, *et al.*, "Proteomic applications for the early detection of cancer," *Nature Reviews Cancer,* vol. 3, pp. 267-275, Apr 2003.

[74] R. Ravindran, *et al.*, "Biochemical Sensing with an Arrayed Silicon Nanowire Platform," *60th Electronic Components and Technology Conference,* pp. 1015-1020, 2010.

[75] P. Verdier-Pinard, *et al.*, "Detection of human beta V-tubulin expression in epithelial cancer cell lines by tubulin proteomics," *Biochemistry,* vol. 44, pp. 15858-15870, Dec 6 2005.

[76] Antoniou, "Average risks of breast and ovarian cancer associated with BRCA1 or BRCA2 mutations detected in case series unselected for family history: A combined analysis of 22 studies (vol 72, pg 1117, 2003)," *American Journal of Human Genetics,* vol. 73, pp. 709-709, Sep 2003.

[77] M. C. King, *et al.*, "Breast and ovarian cancer risks due to inherited mutations in BRCA1 and BRCA2," *Science,* vol. 302, pp. 643-646, Oct 24 2003.

[78] E. Stern, *et al.*, "Label-free Electronic Detection of the Antigen-Specific T-Cell Immune Response," *Nano Letters,* vol. 8, pp. 3310-3314, Oct 2008.

[79] S. Borrello, *et al.*, "Defective Gene-Expression of Mnsod in Cancer-Cells," *Molecular Aspects of Medicine,* vol. 14, pp. 253-258, 1993.

[80] B. S. Kang, *et al.*, "pH measurements with single ZnO nanorods integrated with a microchannel," *Applied Physics Letters,* vol. 86, Mar 14 2005.

[81] A. Kim, *et al.*, "Ultrasensitive, label-free, and real-time immunodetection using silicon field-effect transistors," *Applied Physics Letters,* vol. 91, Sep 3 2007.

[82] N. S. Akulov, "The Theory of Ferromagnetism, Paramagnetism and Ferrimagnetism," *Doklady Akademii Nauk Sssr,* vol. 108, pp. 603-606, 1956.

[83] R. Weissleder, *et al.*, "Ultrasmall Superparamagnetic Iron-Oxide - an Intravenous Contrast Agent for Assessing Lymph-Nodes with Mr Imaging," *Radiology,* vol. 175, pp. 494-498, May 1990.

[84] A. Vacic, *et al.*, "Multiplexed SOI BioFETs," *Biosensors & Bioelectronics,* vol. 28, pp. 239-242, Oct 15 2011.

[85] A. P. Goodey, *et al.*, "Silicon nanowire array photoelectrochemical cells," *Journal of the American Chemical Society,* vol. 129, pp. 12344-+, Oct 17 2007.

[86] K. Q. Peng, *et al.*, "Silicon nanowires for rechargeable lithium-ion battery anodes," *Applied Physics Letters,* vol. 93, Jul 21 2008.

[87] D. M. Jang, *et al.*, "Development and evaluation of 3-D SiP with vertically interconnected through silicon vias (TSV)," *57th Electronic Components & Technology Conference,* pp. 847-852, 2007.

[88] U. Kang, *et al.*, "8 Gb 3-D DDR3 DRAM Using Through-Silicon-Via Technology," *IEEE Journal of Solid-State Circuits,* vol. 45, pp. 111-119, Jan 2010.

[89] F. C. Nix and D. MacNair, "The thermal expansion of pure metals copper, gold, aluminum, nickel, and iron," *Physical Review,* vol. 60, pp. 597-605, Oct 1941.

[90] J. B. Jorcin, *et al.*, "Galvanic coupling between pure copper and pure aluminum experimental approach and mathematical model," *Journal of the Electrochemical Society,* vol. 155, pp. C46-C51, 2008.

[91] R. D. Piner, *et al.*, ""Dip-pen" nanolithography," *Science,* vol. 283, pp. 661-663, Jan 29 1999.

[92] K. Salaita, *et al.*, "Applications of dip-pen nanolithography," *Nature Nanotechnology,* vol. 2, pp. 145-155, Mar 2007.

[93] S. Borkar, "Design Perspectives on 22nm CMOS and Beyond," *Dac: 2009 46th ACM/IEEE Design Automation Conference, Vols 1 and 2,* pp. 93-94, 2009.

[94] K. W. Lee, *et al.*, "Three-Dimensional Hybrid Integration Technology of CMOS, MEMS, and Photonics Circuits for Optoelectronic Heterogeneous Integrated Systems," *IEEE Transactions on Electron Devices,* vol. 58, pp. 748-757, Mar 2011.